Monthly Notices of the ROYAL ASTRONOMICAL SOCIETY

MNRAS **500,** 4514–4529 (2021) doi:10.1093/mnras/staa3589
Advance Access publication 2020 November 20

Clustering dark energy imprints on cosmological observables of the gravitational field

Farbod Hassani [1]★ Julian Adamek [2] and Martin Kunz [1]

[1] *Département de Physique Théorique, Université de Genève, 24 quai Ernest Ansermet, CH-1211 Genève 4, Switzerland*
[2] *School of Physics and Astronomy, Queen Mary University of London, 327 Mile End Road, London E1 4NS, UK*

Accepted 2020 November 11. Received 2020 October 22; in original form 2020 July 20

ABSTRACT

We study cosmological observables on the past light-cone of a fixed observer in the context of clustering dark energy. We focus on observables that probe the gravitational field directly, namely the integrated Sachs–Wolfe and non-linear Rees–Sciama effect (ISW-RS), weak gravitational lensing, gravitational redshift, and Shapiro time delay. With our purpose-built *N*-body code '*k*-evolution' that tracks the coupled evolution of dark matter particles and the dark energy field, we are able to study the regime of low speed of sound c_s where dark energy perturbations can become quite large. Using ray tracing, we produce two-dimensional sky maps for each effect and we compute their angular power spectra. It turns out that the ISW-RS signal is the most promising probe to constrain clustering dark energy properties coded in $w - c_s^2$, as the *linear* clustering of dark energy would change the angular power spectrum by ∼30 per cent at low ℓ when comparing two different speeds of sound for dark energy. Weak gravitational lensing, Shapiro time delay, and gravitational redshift are less sensitive probes of clustering dark energy, showing variations of only a few per cent. The effect of dark energy *non-linearities* in all the power spectra is negligible at low ℓ, but reaches about 2 per cent and 3 per cent, respectively, in the convergence and ISW-RS angular power spectra at multipoles of a few hundred when observed at redshift ∼0.85. Future cosmological surveys achieving per cent precision measurements will allow us to probe the clustering of dark energy to a high degree of confidence.

Key words: dark energy – large-scale structure of Universe – simulations.

1 INTRODUCTION

The accelerated expansion of the Universe that has been attributed to the so-called 'dark energy' component was first discovered using supernova Ia observations over two decades ago independently by Perlmutter et al. (1999) and Riess et al. (1998). Since then, the late-time accelerating expansion has been confirmed by several independent measurements, including the cosmic microwave background (CMB; Spergel et al. 2003; Ade et al. 2016a,b), large-scale structure (Tegmark et al. 2004, 2006), and baryon acoustic oscillations (Percival et al. 2007; Aubourg et al. 2015).

In the Lambda cold dark matter (ΛCDM) standard model of cosmology, the cosmological constant Λ is responsible for the late-time acceleration. Although ΛCDM is a successful model that fits the current data well, Λ is a phenomenological parameter that is not theoretically well motivated and suffers from severe fundamental issues including fine-tuning of the initial energy density and the coincidence problem (see Martin 2012, for a review of the cosmological constant problem). The theoretical issues of the cosmological constant and tensions between some parameters in various cosmological data sets (Handley & Lemos 2019; Verde, Treu & Riess 2019) that have emerged over the past years have motivated cosmologists to propose a plethora of dark energy (in the form of an additional scalar field or 'dark' fluid) and modified gravity models [in the form of a modification of general relativity (GR)] to explain the late-time cosmic acceleration (Clifton et al. 2012; Joyce, Lombriser & Schmidt 2016; Koyama 2018). Since the number of viable dark energy and modified gravity models is substantial, the effective field theory (EFT) approach has been developed and has become popular. It describes the theory economically in the low-energy limit using symmetries and can connect the specific theory to the observation in a straightforward way.

In the near future with high-precision cosmological surveys such as *Euclid* (Laureijs et al. 2011), the Dark Energy Spectroscopic Instrument (Aghamousa et al. 2016), the Legacy Survey of Space and Time (Abate et al. 2012), and the Square Kilometre Array (Santos et al. 2015), we will be able to probe the cosmological models with per cent precision into the highly non-linear regime. One of the main goals of these surveys is to understand the reason behind the cosmic acceleration and to probe the nature of gravity. In the case where the data prefer an alternative dark energy scenario, accurate modelling of the cosmological observables for non-standard models up to highly non-linear scales is required. A very accurate method to model the cosmological predictions of these theories on such scales is obtained using cosmological *N*-body simulations.

Until now several *N*-body codes have been developed for a range of alternative gravity models (Oyaizu, Lima & Hu 2008; Schmidt et al. 2009; Zhao, Li & Koyama 2011; Baldi 2012; Brax et al. 2012; Li et al. 2012; Barreira et al. 2013; Li et al. 2013; Puchwein, Baldi & Springel 2013; Wyman, Jennings & Lima 2013; Llinares, Mota & Winther 2014; Mead et al. 2015; Valogiannis & Bean 2017). These codes are based on Newtonian gravity that is not naturally suited for

★ E-mail: Farbod.Hassani@unige.ch

considering the non-standard dark energy models, therefore requiring a number of approximations. While these may be justified for a crude analysis, the fact that dark energy (as opposed to dark matter) is not dominated by rest-mass density appeals more to a relativistic treatment.

With such applications in mind, some of us have developed GEVOLUTION (Adamek et al. 2016a), an *N*-body code entirely based on GR. One of the main advantages of the GEVOLUTION scheme is that it could be extended naturally to include dark energy or modified gravity models without requiring any approximations in the dark energy sector such as the quasi-static approximation as is done in the Newtonian approaches. A full implementation of the EFT of dark energy encompassing many dark energy and modified gravity models is still a formidable task. As a first step towards this goal, we have recently developed the *k*-evolution code in Hassani et al. (2019) in which we have added a *k*-essence scalar field using the EFT language. Based on GEVOLUTION, some of us have recently also developed *N*-body simulations for parametrized modified gravity in Hassani & Lombriser (2020), and Reverberi & Daverio (2019) have implemented *f*(*R*) models in GEVOLUTION.

In this article, we study the effect of *k*-essence dark energy on the cosmological observables of the gravitational field using our *N*-body codes GEVOLUTION and *k*-evolution. In particular, weak gravitational lensing and the integrated Sachs–Wolfe and Rees–Sciama (ISW-RS) effect probe the gravitational potential and its time derivative directly, and they can be constrained with multiple probes independently. We additionally discuss gravitational redshift and the Shapiro time delay, even though their cosmological detection will be more challenging. We study and quantify the signatures that the *k*-essence model would imprint on each observable.

In Section 2, we discuss the theoretical background, focusing on *k*-essence in the EFT framework of dark energy, and we present the relevant equations that are solved in *k*-evolution to evolve the *k*-essence field. Section 3 is devoted to the general discussion about the cosmological observables and how non-standard dark energy or modified gravity models would affect each observable. The cosmological parameters of our simulations and the way we construct the past light-cone for a fixed observer in our *N*-body codes to make the synthetic sky maps of our observables are explained in Section 4. In Section 5, we show the numerical results from *k*-evolution and GEVOLUTION and we compare the results with the linear theory prediction obtained from the Boltzmann code CLASS. Our conclusions and main take-home points are summarized in Section 6.

2 THEORY

In this section, we briefly review the essentials of the *k*-essence model especially with the focus on its EFT description and the *k*-evolution code, an *N*-body code recently developed to study the evolution of large-scale structure in the presence of a non-linear *k*-essence scalar field; see Hassani et al. (2019) for a description.

To study the evolution of the perturbations around a homogenous flat Friedmann Universe, we consider the Friedmann–Lemaître–Robertson–Walker (FLRW) metric written in the conformal Poisson gauge,

$$\mathrm{d}s^2 = a^2(\tau)[-e^{2\Psi}\mathrm{d}\tau^2 - 2B_i\mathrm{d}x^i\mathrm{d}\tau + (e^{-2\Phi}\delta_{ij} + h_{ij})\mathrm{d}x^i\mathrm{d}x^j], \quad (1)$$

where Ψ and Φ are the Bardeen potentials carrying the scalar perturbations of the metric, B_i is the gravitomagnetic vector perturbation with 2 degrees of freedom as we have $\delta^{ij}\partial_j B_i = 0$, and h_{ij} is the tensor perturbation with the gauge condition $\delta^{ij}h_{ij} = 0 = \delta^{ij}\partial_i h_{jk}$ that results in 2 remaining degrees of freedom.

The *k*-essence model was originally introduced to naturally explain the recent accelerated expansion of the Universe through the idea of a dynamical attractor solution in which this model acts as a cosmological constant at the beginning of the matter-dominated era without any fine-tuning of the parameters (Armendariz-Picon, Mukhanov & Steinhardt 2000, 2001). This model is particularly interesting as it does not rely on coincidence or anthropic reasoning, unlike the cosmological constant and quintessence models[1] in which the energy density today is set by tuning the model parameters.

The *k*-essence action, an action containing at most one single derivative acting on the field, reads

$$S_{\mathrm{DE}} = \int \sqrt{-g}P(X,\varphi)\mathrm{d}^4x, \quad (2)$$

where φ is the scalar field and $X = -\frac{1}{2}g^{\mu\nu}\partial_\mu\varphi\partial_\nu\varphi$ is the kinetic term of the *k*-essence field. In general, we need to choose a specific form for the function $P(X,\varphi)$ to solve the equations of motion for the *k*-essence scalar field. Since there are many possible choices, one can instead employ the EFT approach to model the dynamics of dark energy. EFT, although not a fundamental theory, offers several advantages: First, we can express a large class of dark energy and modified gravity (DE/MG) models with a minimal number of parameters in a model-independent approach and using a unified language. Secondly, the phenomenological parameters of the effective theory can be constrained directly by cosmological observations without being specific to any DE/MG models or to their original motivations. Thirdly, the effective approach allows the theorists to carefully examine the unexplored regions of the space of parameters that could, in principle, guide towards new viable models (Creminelli et al. 2009; Gubitosi, Piazza & Vernizzi 2013).

The EFT framework is a perturbative approach describing a fundamental theory to a certain energy/length-scale. Here, our perturbative expansion is performed in terms of the scalar field. Like the metric perturbations, we assume that the scalar field perturbations remain small over the scales of interest (i.e. cosmological scales). The non-linear regime remains accessible to EFT as long as perturbation theory remains valid [see Frusciante & Papadomanolakis (2017) and Cusin, Lewandowski & Vernizzi (2018) for a discussion about the non-linear extension of the EFT of DE framework]. For example, for the case of *k*-essence theory, we have shown in Hassani et al. (2019) that based on our EFT scheme, highly non-linear scalar field configurations are allowed to form while still respecting the weak field approximation. The main difference between the fundamental theory and its EFT description is that the scalar field can become arbitrarily large in the former while it has to remain perturbatively small in the latter. The upshot is that the EFT framework allows one to study the infrared phenomenology without having to specify the ultraviolet completion of the theory in the first place.

In *k*-evolution (Hassani et al. 2019), which is an extension of GEVOLUTION (Adamek et al. 2016a,b) in which we have implemented the *k*-essence model as a dark energy sector, we use the EFT approach to write down the equations of motion parametrized with the equation of state w and the squared speed of sound c_{s}^2. They are related to the general action of equation (2) as

$$w = \frac{P}{2XP_{,X} - P}, \quad c_{\mathrm{s}}^2 = \frac{P_{,X}}{2XP_{,XX} + P_{,X}}, \quad (3)$$

[1]The quintessence model is a canonical scalar field model, corresponding to the special case of the *k*-essence model where the kinetic term is canonical.

where $P_{,X} \doteq \partial P/\partial X$ and one has to evaluate the expressions on the background solution of φ (Armendariz-Picon, Damour & Mukhanov 1999; Bonvin, Caprini & Durrer 2006). These phenomenological parameters completely characterize the low-energy limit of the theory. Of course, w and c_s^2 do not uniquely fix the function $P(X, \varphi)$ and in this work we will not consider the question of finding suitable choices. Explicit examples have been studied, for example, in Chiba, Okabe & Yamaguchi (2000), Armendariz-Picon et al. (1999, 2001), Malquarti et al. (2003), Wei & Cai (2005), Rendall (2006), de Putter & Linder (2007), Silverstein & Tong (2004), Alishahiha, Silverstein & Tong (2004), Fang, Lu & Huang (2007), and Kang, Vanchurin & Winitzki (2007).

The scalar field evolution, keeping only linear terms of the scalar field and its time derivative, is given by

$$\pi' = \zeta - \mathcal{H}\pi + \Psi, \tag{4}$$

$$\zeta' = 3w\mathcal{H}\zeta - 3c_s^2(\mathcal{H}^2\pi - \mathcal{H}\Psi - \mathcal{H}'\pi - \Phi') + c_s^2\nabla^2\pi, \tag{5}$$

where π is the scalar field perturbation around its background value, ζ is written in terms of π and π', $\nabla^2 = \delta^{ij}\partial_i\partial_j$, a prime $'$ denotes the time derivative with respect to the conformal time, and $\mathcal{H}$ is the conformal Hubble function. The linear stress energy tensor reads

$$\begin{aligned} T_0^0 &= -\rho + \frac{\rho + p}{c_s^2}\left(3c_s^2\mathcal{H}\pi - \zeta\right), \\ T_i^0 &= -(\rho + p)\partial_i\pi, \\ T_j^i &= p\delta_j^i - (\rho + p)(3w\mathcal{H}\pi - \zeta)\delta_j^i. \end{aligned} \tag{6}$$

It is worth noting that in connection with the EFT language, with the notation used in Gleyzes et al. (2013), apart from the background parameters $\Lambda(t)$ and $c(t)$ the only remaining parameter in EFT for k-essence theory is $M_2^4(t)$. In the alternative EFT notation using $\alpha_i(t)$ explained in Bellini & Sawicki (2014), α_K is the only non-zero parameter.

The detection of the binary neutron star merger GW170817 and its electromagnetic counterpart (Abbott et al. 2017) implies that gravitational waves propagate at the speed of light with uncertainties of about 5×10^{-16}. This result puts strong constraints on dark energy and modified gravity theories (Baker et al. 2017; Creminelli & Vernizzi 2017; Ezquiaga & Zumalacárregui 2017; Sakstein & Jain 2017; Copeland et al. 2019). The speed of gravitational waves is modified in any theory that features a non-vanishing α_T parameter, which is now observationally strongly disfavoured. However, this constraint does not affect the k-essence model because, as we just pointed out, only α_K is non-zero in this model.

As discussed in Hassani et al. (2019), although we keep only linear terms in the scalar field dynamics and we drop higher order self-interactions of π, the scalar field does cluster and form non-linear scalar field structures in k-evolution because it is sourced by non-linearities in matter through gravitational coupling. This is the crucial improvement over the treatment of dark energy in GEVOLUTION, which uses the transfer functions from linear theory to keep track of perturbations in the dark energy fluid similar to how it is done in Dakin et al. (2019) (see also Brando, Koyama & Wands 2020, for a more comprehensive extension of this framework to EFT).

Einstein's equations for the evolution of the scalar perturbations in the weak field regime (Adamek, Durrer & Kunz 2017a) read

$$(1 + 2\Phi)\nabla^2\Phi - 3\mathcal{H}\Phi' - 3\mathcal{H}^2\Psi - \frac{1}{2}\delta^{ij}\partial_i\Phi\partial_j\Phi = -4\pi G a^2\delta T_0^0, \tag{7}$$

$$\begin{aligned} &\nabla^4(\Phi - \Psi) - \left(3\delta^{ik}\delta^{jl}\frac{\partial^2}{\partial x^k\partial x^l} - \delta^{ij}\nabla^2\right)\partial_i\Phi\partial_j\Phi \\ &\quad = 4\pi G a^2\left(3\delta^{ik}\frac{\partial^2}{\partial x^j\partial x^k} - \delta_j^i\nabla^2\right)T_i^j, \end{aligned} \tag{8}$$

where the stress tensor T_μ^ν includes all the relevant species, i.e. matter, dark energy, and radiation.

In Hassani et al. (2019), we introduce k-evolution and the full non-linear equations for the k-essence model written using the EFT action. We study the dark energy clustering and its impact on the large-scale structure of the Universe. Moreover, we discuss that the scalar dark energy does not lead to significantly larger vector and tensor perturbations than ΛCDM. Thus, one can safely neglect the vector and tensor perturbation in this theory. In Hassani et al. (2020), we quantify the non-linear effects from k-essence dark energy through the effective parameter $\mu(k, z)$ that encodes the contribution of a dark energy sector to the Poisson equation (see below). We also show that for the k-essence model the difference between the two potentials $\Phi - \Psi$ and short-wave corrections appearing as higher order terms in the Poisson equation can be safely neglected. Moreover, in Hansen et al. (2020), we study the effect of k-essence dark energy as well as some other modified gravity theories on the turnaround radius – the radius at which the inward velocity due to the gravitational attraction and outward velocity due to the expansion of the Universe cancel each other – in galaxy clusters.

It is sometimes useful to parametrize the effect that clustering dark energy has on the gravitational potential phenomenologically through a modified Poisson equation,

$$-k^2\Phi = 4\pi G_N a^2\mu(k, z)\sum_X \bar{\rho}_X\Delta_X, \tag{9}$$

where Δ is the comoving density contrast and the species X do not include the dark energy field. Denoting in addition the ratio between the two Bardeen potentials as

$$\eta(k, z) = \frac{\Psi(k, z)}{\Phi(k, z)}, \tag{10}$$

one obtains a phenomenological classification of DE/MG models through two generic functions of time and scale, with ΛCDM predicting $\eta = \mu = 1$ everywhere (e.g. Ade et al. 2016b; Blanchard et al. 2019). As discussed in Hassani et al. (2020), for the case where k-essence plays the role of dark energy, $\eta(k, z) \approx 1$ and $\mu(k, z)$ is fitted well with a tanh function where the amplitude and shape of the function depend on the speed of sound and equation of state. In Hassani et al. (2020), we studied the difference between μ from linear and non-linear treatments, and we have shown that for high speed of sound one would get similar μ in both cases, but for low speed of sound there is an effect coming from the scalar field non-linearities that should be taken into account. Here, the speed of sound is considered 'low' if the corresponding sound horizon lies at a non-linear scale.

For the sake of completeness, we show the effect of k-essence, expressed in the form of $w - c_s^2$ in the parameter space, on the background evolution and the growth of matter density perturbation. The effect of k-essence appears on the background evolution via the equation of state but independent of the speed of sound of dark energy. We show the conformal Hubble parameter $\mathcal{H}$ as well as the redshift–distance relation in Fig. 1 in the left-hand and middle panels for wCDM with $w = -0.9$ and ΛCDM, which are the cases we consider in this article. We also compare the logarithmic growth rate $f = \mathrm{dln}\,\Delta_m/\mathrm{dln}\,a$ in the right-hand panel of Fig. 1 for different scenarios to see the impact of different choices of w and c_s^2 on the growth of

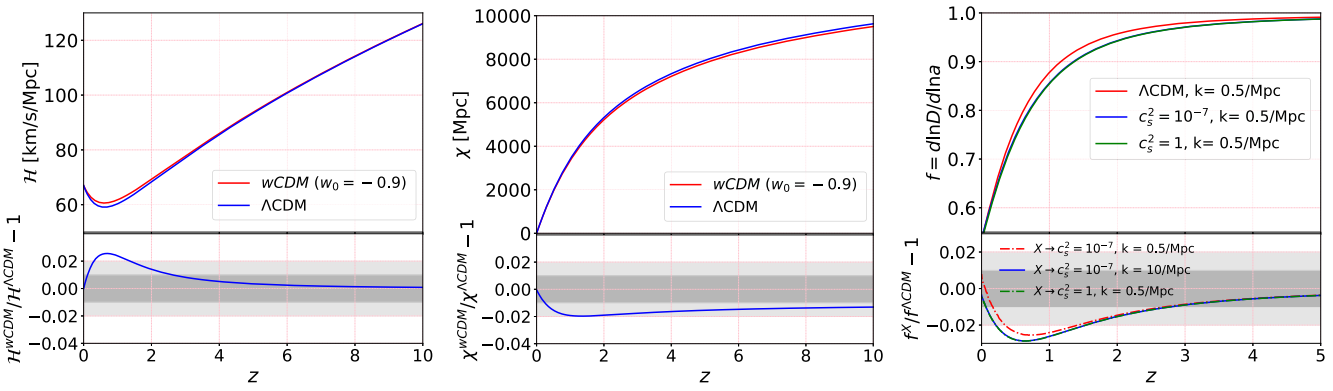

Figure 1. Left: The conformal Hubble parameter as a function of redshift for ΛCDM and wCDM with $w_0 = -0.9$. In the bottom panel, we show the relative difference. As expected, the effect of dark energy goes away at high redshifts. Centre: The comoving distance as a function of redshift for the two cosmologies is plotted. In the bottom panel, again the relative difference is shown. The relative difference asymptotes to a constant at high redshifts because the comoving distance is an integrated quantity. Right: In the top panel, the logarithmic growth rate f as a function of redshift for a fixed wavenumber is plotted. In the bottom panel, the relative difference between different scenarios is shown with respect to ΛCDM. While in the latter case the growth rate is scale independent (neglecting corrections due to neutrinos), in a clustering dark energy model the behaviour of a mode depends on whether it is inside or outside of the sound horizon. We compare three cases with ΛCDM, namely the mode $k = 0.5$ Mpc^{-1} with $c_s^2 = 10^{-7}$, $k = 10$ Mpc^{-1} with $c_s^2 = 10^{-7}$, and $k = 0.5$ Mpc^{-1} with $c_s^2 = 1$. Only the first case corresponds to a mode outside the sound horizon, while the other two are well inside. Thus, we see the same behaviour for $k = 10$ Mpc^{-1} with $c_s^2 = 10^{-7}$ and $k = 0.5$ Mpc^{-1} with $c_s^2 = 1$.

structures. The logarithmic growth rate provides a useful way to distinguish between DE/MG gravity and ΛCDM (Kunz & Sapone 2007; Dossett & Ishak 2013; Amendola et al. 2018; Blanchard et al. 2019).

Since the logarithmic growth rate is in general scale dependent, we compute it for different scales by studying the evolution of the comoving matter density contrast Δ_m, which we define for this purpose through $\Omega_m\Delta_m = \Omega_b\Delta_b + \Omega_{cdm}\Delta_{cdm}$. We compute Δ_m with the linear Boltzmann code CLASS and look at the evolution for wavenumbers $k = 0.5$ and 10 Mpc^{-1} for the model with $c_s^2 = 10^{-7}$ that corresponds, respectively, to a mode well outside and a mode well inside the sound horizon. We compare the logarithmic growth rate from the two modes for $c_s^2 = 10^{-7}$, and in addition $k = 0.5$ Mpc^{-1} for $c_s^2 = 1$, with ΛCDM in the bottom right panel of Fig. 1. As expected, for the mode $k = 0.5$ Mpc^{-1} in the case where $c_s^2 = 1$, as it is well inside the sound horizon, the result matches with the mode evolution of $k = 10$ Mpc^{-1} in the case where $c_s^2 = 10^{-7}$. The mode $k = 0.5$ Mpc^{-1} has a different evolution in the case where $c_s^2 = 10^{-7}$ because it is outside the sound horizon and the perturbations in the dark energy field are therefore not suppressed.

3 OBSERVABLES

Solving the null geodesic equation ($k^\mu\nabla_\mu k_\nu = 0$) for a light ray with wavevector k^μ in a perturbed FLRW universe results in a change in position and energy of the light beam emitted from the source. The apparent comoving 3D position of the source reads (Yoo, Fitzpatrick & Zaldarriaga 2009; Bonvin & Durrer 2011; Challinor & Lewis 2011; Breton et al. 2019; Adamek et al. 2020)

$$\boldsymbol{s} = \chi_s\boldsymbol{n} + \underbrace{\frac{1}{H_s(\bar{z})}\delta z\,\boldsymbol{n}}_{\text{redshift perturbation}} - \underbrace{\int_0^{\chi_s}(\chi_s-\chi)\nabla_\perp(\Phi+\Psi)\mathrm{d}\chi}_{\text{weak gravitational lensing}} - \underbrace{\boldsymbol{n}\int_0^{\chi_s}(\Phi+\Psi)\mathrm{d}\chi}_{\text{Shapiro time delay}}, \tag{11}$$

where $\boldsymbol{s}$ is the observed position in redshift space, and $\boldsymbol{n}$ and χ_s are, respectively, the unperturbed direction vector and unperturbed comoving distance to the source. Furthermore, $\nabla_\perp \equiv (\mathbb{1} - \boldsymbol{n}\otimes\boldsymbol{n})\nabla$ is the projected gradient perpendicular to the line of sight, χ is the comoving distance, and $H_s(\bar{z})$ is the Hubble rate at the unperturbed redshift $\bar{z}$ of the source. The first term in equation (11) corresponds to the unperturbed position, the second term corresponds to the redshift perturbation that is computed in equation (12), the third term (weak gravitational lensing) yields an angular deflection of the source position on the 2D sphere, and the last term changes the radial position due to the Shapiro time delay.

Using the time component of geodesic equation, one obtains the redshift perturbation $\delta z = z - \bar{z}$ as

$$\delta z = (1+\bar{z})\left[\underbrace{\boldsymbol{n}\cdot(\boldsymbol{v}_s-\boldsymbol{v}_o)}_{\text{Doppler}} + \underbrace{\Psi_o-\Psi_s}_{\substack{\text{gravitational}\\ \text{redshift}}} - \underbrace{\int_0^{\chi_s}\frac{\partial(\Psi+\Phi)}{\partial\tau}\mathrm{d}\chi}_{\text{ISW-RS effect}}\right]. \tag{12}$$

As a result of equations (11) and (12), the light ray along its path is deflected, redshifted, and delayed due to the different physical phenomena, namely weak gravitational lensing, ISW-RS effect, and Shapiro time delay. In addition, there are two local (non-integrated) contributions to the redshift: the relativistic Doppler effect (due to the peculiar velocities $\boldsymbol{v}_s$ and $\boldsymbol{v}_o$ of the source and observer, respectively) and the gravitational redshift (ordinary Sachs–Wolfe effect). Among these, the weak gravitation lensing, ISW-RS, Shapiro time delay, and gravitational redshift all depend directly on the configuration of the gravitational field. If they can be observed independently, they can be used as a probe of DE/MG. In this work, we are going to look at each individual aforementioned effect to study the impact of k-essence clustering dark energy. It is important to point out that the Doppler term is also expected to be a powerful probe of dark energy and is worth to be studied in detail. However, in this paper we only focus on the physical effects coming from the metric perturbations Ψ and Φ. These have the advantage that they can be observed (as integrated effects) even in places where there are no visible sources, like in voids that are naturally expected to be dominated by dark energy.

In the following sections, we shall introduce and derive the relevant expressions for each effect separately and we will discuss why each

of these observables could be potentially used to put constraint on DE/MG models, especially clustering dark energy.

3.1 Weak gravitational lensing

The light from distant objects is deflected due to inhomogeneities as it travels through the intervening large-scale structure in the Universe. The deflection angles are usually small at cosmological scales and this phenomenon is called weak gravitational lensing. As mentioned already, weak gravitational lensing directly probes the distribution of matter and energy, including dark matter and dark energy, which makes it a unique tool to constrain the cosmological parameters (Bartelmann & Schneider 2001; Refregier 2003; Lewis & Challinor 2006; Ade et al. 2014a; Hassani, Baghram & Firouzjahi 2016; Hikage et al. 2019). Weak gravitational lensing can be observed through the statistics of cosmic shear and cosmic convergence, as we will summarize briefly in the following.

Cosmic shear refers to the change of the ellipticities of galaxies observed on the far side of the gravitational lens. The cosmic convergence, on the other hand, magnifies/demagnifies the sizes and magnitudes of the same galaxies (Alsing et al. 2015; Mandelbaum 2018). The first detection of cosmic shear has been done about 20 yr ago (Bacon, Refregier & Ellis 2000; Van Waerbeke et al. 2000), while cosmic convergence was measured for the first time in 2011 (Schmidt et al. 2012). Since then, the precision in cosmic shear and cosmic convergence measurements has been improved and these two have become some of the most promising probes of dark energy and modified gravity (Jain & Taylor 2003; Hannestad, Tu & Wong 2006; Amendola, Kunz & Sapone 2008; Spurio Mancini et al. 2018).

In Adamek et al. (2019), some of us have implemented a ray-tracing method to analyse relativistic *N*-body simulations performed with the code GEVOLUTION. In this method, one solves the optical equations in the scalar sector of gravity without any approximation and additionally keeps track of the frame dragging to first order. Weak-lensing convergence and shear obtained with this numerical method were studied in more detail in Lepori et al. (2020). While other approaches often try to reconstruct the signal from the mass distribution, our method works with the metric perturbations directly and is therefore more robust once we consider DE/MG like in this work. To this end, we have recently implemented the same light-cone analysis and ray-tracing method in *k*-evolution. Here, however, we compute each effect only to first order in Φ and Ψ, and we neglect the frame dragging. For the purpose of discussing angular power spectra, this is sufficient, as non-perturbative effects (in the ray tracing[2]) would only enter at a detectable level for very high multipoles that are not resolved in our maps.

In the first-order weak gravitational lensing formalism, one introduces the lensing potential $\psi(\boldsymbol{n}, z)$, defined as

$$\psi(\boldsymbol{n}, z) \equiv -\int_0^{\chi_s} \mathrm{d}\chi \, \frac{\chi_s - \chi}{\chi_s \chi} (\Phi + \Psi) \,, \tag{13}$$

where the redshift z and the source distance χ_s are related through the background distance–redshift relation, and the integration is carried out in direction $\boldsymbol{n}$ using the Born approximation.

Using the gradient $\hat{\nabla}^a$ on the 2D sphere, we can calculate the deflection angle as $\alpha^a = \theta_o^a - \theta_s^a = \hat{\nabla}^a \psi$, which results in the lensing term in equation (11). The Jacobi map, which is a map between the unperturbed source angular positions θ_s and the observed angular positions θ_o, i.e. $\mathcal{A}_{ab} = \partial \theta_o^a / \partial \theta_s^b$, contains the full information for weak gravitational lensing and reads

$$\mathcal{A} = \begin{pmatrix} 1 - \kappa - \gamma_1 & \omega - \gamma_2 \\ -\omega - \gamma_2 & 1 - \kappa + \gamma_1 \end{pmatrix}, \tag{14}$$

which at leading order is rewritten in terms of the gradients of the lensing potential,

$$\mathcal{A} = \mathbb{1} + \left(\hat{\nabla}_a \hat{\nabla}_b \psi \right). \tag{15}$$

Note that this also implies $\omega = 0$ at leading order. We can extract the convergence κ and the complex shear from the lensing potential as

$$\kappa = -\frac{1}{2} \hat{\nabla}^2 \psi, \tag{16}$$

$$\gamma \equiv \gamma_1 + i\gamma_2 = -\frac{1}{2} \left(\hat{\nabla}_1^2 - \hat{\nabla}_2^2 \right) \psi - \mathrm{i} \hat{\nabla}_1 \hat{\nabla}_2 \psi. \tag{17}$$

The relation between a non-perturbative geometrical description and these first-order quantities is discussed in detail in Lepori et al. (2020).

The lensing potential, convergence, and complex shear as scalar functions on the 2D sphere may be expanded on the basis of spherical harmonics $Y_{\ell m}(\boldsymbol{n})$,

$$X(\boldsymbol{n}) = \sum_{\ell m} X_{\ell m} Y_{\ell m}(\boldsymbol{n}). \tag{18}$$

Assuming that these functions obey statistical isotropy, the two-point function of the expansion coefficients $X_{\ell m}$ is diagonal in ℓ and m and we can define the angular power spectrum C_ℓ as

$$\langle X_{\ell m} X_{\ell' m'} \rangle \equiv \delta_{\ell \ell'} \delta_{m m'} C_\ell^X. \tag{19}$$

Our code uses directly equation (13) to construct the lensing map and then computes the angular power spectrum from the map. We can, however, also compute an expression for the weak-lensing C_ℓ^κ by considering the two-point function of the integrand of equation (13) and using equation (16) in harmonic space,

$$C_\ell^\kappa = 4\pi^2 \ell^2 (\ell+1)^2 \int_0^\infty k^2 \mathrm{d}k \int_0^{\chi_s} \mathrm{d}\chi \, \frac{\chi_s - \chi}{\chi_s \chi} \int_0^{\chi_s} \mathrm{d}\chi' \, \frac{\chi_s - \chi'}{\chi_s \chi'} \times \left[1 + \eta(k, \chi)\right] \left[1 + \eta(k, \chi')\right] j_\ell(k\chi) j_\ell(k\chi') P_\Phi(k, \chi, \chi'), \tag{20}$$

where $P_\Phi(k, \chi, \chi')$ is the unequal-time correlator of the gravitational potential in Fourier space defined by

$$\langle \Phi(\boldsymbol{k}, \chi) \Phi^*(\boldsymbol{k}', \chi') \rangle = (2\pi)^3 \delta_{\mathrm{D}}(\boldsymbol{k} - \boldsymbol{k}') P_\Phi(k, \chi, \chi'). \tag{21}$$

Moreover, according to equation (9) the gravitational potential unequal-time correlator may be written based on the one of matter as follows:

$$P_\Phi(k, \chi, \chi') = k^{-4} \left(4\pi G_N \bar{\rho}_m^0 \right)^2 \mu(k, \chi) \mu(k, \chi') \times [1 + \bar{z}(\chi)][1 + \bar{z}(\chi')] P_{\Delta_m}(k, \chi, \chi'). \tag{22}$$

In the last few equations, we use the shorthand $\mu(k, \chi)$ for $\mu[k, z(\chi)]$ and similarly for η, P_Φ, and so on.

The lensing signal, as a result, responds to the DE/MG models in multiple ways: at the background level through a change in the distance–redshift relation, and at the level of perturbations through a modified growth and through the modifications encoded in the $\mu(k, z)$ and $\eta(k, z)$ parameters (Takahashi et al. 2017; Spurio Mancini et al. 2018), specifically through the combination $\Sigma = \mu(1 + \eta)/2$ that describes the modification of the lensing potential (Amendola et al.

[2]We remind the reader that Φ and Ψ themselves represent non-perturbative solutions obtained with full simulations.

2008). In Section 5, we will compute the lensing signal for two fixed source redshifts, namely $z = 0.85$ and 3.3, in N-body simulations to study the effects of dark energy clustering and of the expansion history on the lensing.

It is also worth mentioning that at leading order in the absence of systematics and shape noise (Köhlinger et al. 2017) the convergence angular power spectrum contains the full lensing information. Decomposing the shear into rotationally invariant E and B components, one can show from equation (15) that (Becker 2013)

$$C_\ell^{\gamma_{\rm E}} = \frac{1}{\ell^2(\ell+1)^2}\frac{(\ell+2)!}{(\ell-2)!}C_\ell^{\kappa},$$
$$C_\ell^{\gamma_{\rm B}} = \frac{1}{\ell^2(\ell+1)^2}\frac{(\ell+2)!}{(\ell-2)!}C_\ell^{\omega} = 0. \quad (23)$$

In the following sections, we therefore only discuss the convergence power spectra.

3.2 Integrated Sachs–Wolfe and non-linear Rees–Sciama effect

If the light rays from source galaxies traverse a time-dependent gravitational potential, then in general their energy will change (Sachs & Wolfe 1967). Specifically, the light is redshifted for rays passing through a growing potential well, and blueshifted if the potential well is decaying. This effect is known as late integrated Sachs–Wolfe effect (late ISW) and is a powerful probe of dark energy at low multipoles.

During matter domination and in linear perturbation theory, the gravitational potential wells remain constant in time and as a result the photons do not gain or lose energy along their trajectories after accounting for the expansion of the background. However, when dark energy becomes important and the expansion rate of the Universe deviates from the matter-dominated behaviour, the gravitational potential decays at linear scales. As a result, photons gain energy and are blueshifted as they travel through overdense regions while they lose energy and are redshifted as they travel through voids (Ade et al. 2016b; Carbone, Petkova & Dolag 2016). In this way, the late ISW effect induces additional anisotropies in the power spectrum of the CMB radiation, primarily at large scales. These anisotropies are correlated with the large-scale structure as they are due to evolving gravitational potential wells.

In addition to this effect in linear perturbation theory, the perturbations on small scales and at late times evolve non-linearly. The non-linear large-scale structure of the Universe induces additional energy changes in the light rays as they pass through these structures. This so-called Rees–Sciama effect (Rees & Sciama 1968) enhances the ISW effect in underdense regions and decreases it in the overdense regions as the non-linear growth of structure acts opposed to dark energy (Cai et al. 2010).

The linear late ISW and non-linear Rees–Sciama effects (abbreviated as ISW-RS when combined) are sensitive to the background evolution and growth of structures at late times, when the dark energy dominates over other components (Cabass et al. 2015; Khosravi, Mollazadeh & Baghram 2016; Beck et al. 2018; Adamek et al. 2020).

Direct measurements of the ISW-RS signal from CMB data are demanding, and as a result it is detected indirectly, either by cross-correlating large-scale structure data and CMB maps (Seljak 1996; Peiris & Spergel 2000; Scranton et al. 2003; Francis & Peacock 2010; Ade et al. 2016c) or by stacking clusters and voids to enhance the signal (Granett, Neyrinck & Szapudi 2008; Cai et al. 2014, 2017; Ade et al. 2016c). The effect is also detected through the ISW-lensing bispectrum using the Planck data (Ade et al. 2014b).

According to equation (12), the term responsible for the ISW-RS effect yields a change in CMB temperature,

$$\Theta(\boldsymbol{n}, z) \equiv \frac{\Delta T}{\bar{T}} = -\frac{\delta z}{1+\bar{z}} = \int_0^{\chi_{\rm s}} \frac{\partial(\Psi+\Phi)}{\partial\tau}\,{\rm d}\chi, \quad (24)$$

where $\chi_{\rm s}$ is the distance to the last-scattering surface for the CMB. In the presence of DE/MG, the gravitational potentials Φ and Ψ are modified as a result of equations (9) and (10) for the gravitational slip and clustering parameters $\eta(k, z)$, $\mu(k, z)$. It is also interesting to note that these modifications are projected in a different way for the ISW-RS signal and the lensing signal, and thus these two could probe DE/MG in independent ways. Following the discussion in the previous section, $\Theta(\boldsymbol{n}, z)$ may be expanded in terms of spherical harmonics and one can compute the ISW-RS angular power spectrum. Taking the time derivative of the Hamiltonian constraint (the modified Poisson equation) (9), and replacing Ψ through (10), results in a constraint equation for $\partial(\Phi+\Psi)/\partial\tau$ that in general is a function of $\mu(k, z)$, $\eta(k, z)$ and their time derivatives:

$$\frac{\partial(\Phi+\Psi)}{\partial\tau} = 4\pi G_N a^2 \bar{\rho}_{\rm m}\Delta_{\rm m}\frac{H(z)}{k^2}\left[\mu(k,z)\frac{\partial\eta(k,z)}{\partial z} - (1+\eta(k,z)) \times\left(\mu(k,z)\frac{f(k,z)-1}{1+z} - \frac{\partial\mu(k,z)}{\partial z}\right)\right]. \quad (25)$$

Writing this as $\partial(\Phi+\Psi)/\partial\tau = g(k, z)\Delta_{\rm m}$, we find

$$C_\ell^{\Theta} = 16\pi^2\int_0^\infty k^2{\rm d}k\int_0^{\chi_{\rm s}}{\rm d}\chi\int_0^{\chi_{\rm s}}{\rm d}\chi' j_\ell(k\chi)j_\ell(k\chi') \times g(k,\chi)g(k,\chi')P_{\Delta_{\rm m}}(k,\chi,\chi'). \quad (26)$$

In this article, we use ray tracing to compute the ISW-RS signal according to equation (24) by integrating along the past light-cone to the source redshifts $z = 0.85$ and 3.3 as in the previous section. This can be seen either as a direct contribution to the observed redshift of the sources or as a fractional contribution to the CMB temperature anisotropy that captures the part of the signal that is generated by the structure out to that distance and that could therefore be constrained through a cross-correlation of the CMB with large-scale structure. We use the ISW-RS angular power spectra in Section 5 to measure the response of this signal to different k-essence scalar field scenarios.

3.3 Gravitational redshift

The light rays emitted from source galaxies in the potential well of galaxy clusters and dark matter haloes are expected to be redshifted/blueshifted due to the difference in gravitational potential between the source galaxy and the observer. This effect is known as gravitational redshift (Cappi 1995) or as ordinary Sachs–Wolfe effect in the context of CMB physics (Durrer 2001), and is the second term in the full expression written in equation (12),

$$\delta z_{\rm grav} = (1+\bar{z})(\Psi_{\rm o} - \Psi_{\rm s}). \quad (27)$$

For typical cluster masses (of the order of $\sim 10^{14}$ $M_\odot$), the gravitational redshift is estimated to be two orders of magnitude smaller than the Doppler shift [the first term in equation (12)] coming from the random motion of source galaxies (Cappi 1995). The technique to extract the gravitational redshift signal from other dominant signals depends on the fact that the Doppler shift results in a symmetric dispersion in the redshift-space distribution, while the gravitational redshift changes the mean of the distribution (Broadhurst & Scannapieco 2000; Kim & Croft 2004). In Wojtak, Hansen & Hjorth (2011), the first measurement of gravitational redshift of light coming from galaxies in clusters was carried out

by stacking 7800 clusters from the Sloan Digital Sky Survey survey in redshift space. The signal detection was used to rule out models avoiding the presence of dark matter and also to show the consistency of the results with the predictions of GR. The gravitational redshift signal was detected [e.g. in Sadeh, Feng & Lahav (2015) and Jimeno et al. (2015)] on scales of a few Mpc around galaxy clusters and recently in elliptical galaxies (Zhu et al. 2019) using spectra from the Mapping Nearby Galaxies at Apache Point Observatory experiment.

The gravitational redshift as an observable is a prominent and direct probe of gravity at cosmological scales (Wojtak et al. 2011; Alam et al. 2017). We expect to see the effect of dark energy perturbations directly in the gravitational redshift signal since $\Psi \propto \mu(k, z)\eta(k, z)\Delta_{\rm m}$; see equations (9) and (10). Hence,

$$C_\ell^{\delta z_{\rm grav}} = 36\pi^2 H_0^4 \Omega_{\rm m}^2 [1+\bar{z}(\chi_{\rm s})]^4 \times \int_0^\infty \frac{{\rm d}k}{k^2} j_\ell^2(k\chi_{\rm s})\mu^2(k,\chi_{\rm s})\eta^2(k,\chi_{\rm s})P_{\Delta_{\rm m}}(k,\chi_{\rm s}). \quad (28)$$

In Section 5, we study the effect of k-essence dark energy on the gravitational redshift signal.

3.4 Shapiro time delay

In addition to all the effects discussed in the previous sections, the gravitational potential of large-scale structure perturbs the interval of cosmic time while a photon traverses a given coordinate distance. This effect is known as Shapiro time delay and is first discussed and introduced in Shapiro (1964) as a fourth test of GR.

While the gravitational lensing is due to the gradient of the projected potentials along the photon trajectories and is weighted by the lensing kernel, the Shapiro time delay is proportional to the projected potential itself. As a result, we expect much more signal at high multipoles from the lensing convergence compared to the Shapiro time delay, due to the additional factor of $\sim\ell^2$.

Due to Shapiro time delay, the last scattering surface is a deformed sphere as different light rays travel through different gravitational potentials to reach us. All the photons we receive from the last scattering surface were released almost at the same time, so the time delay means that the photons reaching us from different directions have started at different distances from us. The modulation of the spherical surface due to Shapiro time delay is $\sim$1 Mpc (Hu & Cooray 2001). The effect of Shapiro time delay on the CMB temperature and polarization anisotropies is studied in Hu & Cooray (2001). They show that, while it is difficult to extract the Shapiro time delay signal from the data, neglecting it would introduce a systematic error. They argue that the Shapiro time delay should be considered in order to reduce the systematics in the analysis, especially for future high-precision experiments.

In Li, Dodelson & Hu (2019), an estimator quadratic in the temperature and polarization fields is introduced to provide a map of the Shapiro time delays as a function of position on the sky. They show that the signal-to-noise ratio of this map could exceed unity for the dipole, so the signal could be used to provide an understanding of the Universe on the largest observable scales.

As discussed in Nusser (2016), for tests of the equivalence principle at high redshift that rely on the Shapiro time delay effect, potential fluctuations from the large-scale structure of the Universe are at least two orders of magnitude larger than the gravitational potential of the Milky Way. This suggests that the effect of dark energy on these potentials needs to be considered in order to model the Shapiro time delay accurately. From the last term in equation (11), we get

$$\Delta\tau = (1+\bar{z})\,\Delta t = -\int_0^{\chi_{\rm s}} (\Phi+\Psi){\rm d}\chi, \quad (29)$$

and hence

$$C_\ell^{\Delta\tau} = 16\pi^2 \int_0^\infty k^2{\rm d}k \int_0^{\chi_{\rm s}} {\rm d}\chi \int_0^{\chi_{\rm s}} {\rm d}\chi' j_\ell(k\chi) j_\ell(k\chi') \times [1+\eta(k,\chi)][1+\eta(k,\chi')]P_\Phi(k,\chi,\chi'). \quad (30)$$

The dependence on $\mu(k, z)$ is evident from equation (22). This expression can be compared to equation (20) where dark energy enters identically in the integrand, but the effect is weighted differently along the line of sight due to the lensing kernels. In our numerical analysis, we obtain sky maps of the Shapiro time delay by directly solving equation (29).

4 SIMULATIONS

The results presented in this paper are based on simulations performed with the relativistic N-body codes k-evolution (Hassani et al. 2019), which includes non-linearly clustering dark energy in the form of a k-essence scalar field, and GEVOLUTION (Adamek et al. 2016a) for ΛCDM and cases where linear dark energy perturbations are sufficient (see fig. 1 in Hassani et al. 2019). We also compare our results from these two N-body codes with the linear Boltzmann code CLASS (Blas, Lesgourgues & Tram 2011).

In GEVOLUTION and k-evolution, for a fixed observer, a 'thick' approximate past light-cone is constructed that encompasses a region sufficiently large to permit the reconstruction of the true light-cone following the deformed photon trajectories in post-processing (Adamek et al. 2019). The metric information for this thick light-cone is saved in spherical coordinates pixelized using HEALPIX (Gorski et al. 2005). This lets us compute light-cone observables including weak gravitational lensing, ISW-RS, Shapiro time delay, and gravitational redshift in post-processing. In this work, we use a fast pixel-based method to solve the integrals of equations (13), (24), and (29) in the Born approximation, given that post-Born corrections typically affect the angular power spectra only at very high multipoles. A comparison of this approach with 'exact' ray tracing of the deformed geodesics is presented in Lepori et al. (2020) for the case of the weak-lensing convergence (see also Pratten & Lewis 2016) and justifies the use of the Born approximation for the multipoles discussed here. Note, however, that post-Born corrections can play an important role in higher order correlation functions like the angular bispectrum.

For illustration, in Fig. 2 the maps of each physical effect from a ΛCDM simulation are shown in the left-hand panels. In the right-hand panels, the difference between the maps from k-essence with $w_0 = -0.9$ and $c_{\rm s}^2 = 10^{-7}$ and k-essence with $w_0 = -0.9$ and $c_{\rm s}^2 = 1$ is shown. Since the seed number of the simulations are identical, this shows the effect of k-essence clustering on each map, because k-essence does not cluster significantly for the case with high speed of sound squared, $c_{\rm s}^2 = 1$.

In our simulations, we place the observer in the corner of the box at position (0, 0, 0) in Cartesian coordinates. We store data on the past light-cone of the observer on the full sky out to a comoving distance of $\chi_{\rm s} = 2015\,{\rm Mpc}\,h^{-1}$, which corresponds approximately to $z = 0.8$, and out to a comoving distance of $\chi_{\rm s} = 4690\,{\rm Mpc}\,h^{-1}$ or a corresponding approximate redshift of $z = 3.3$ for a pencil beam covering a sky area of 1932 sq. deg. in the direction of the diagonal of the simulation box.

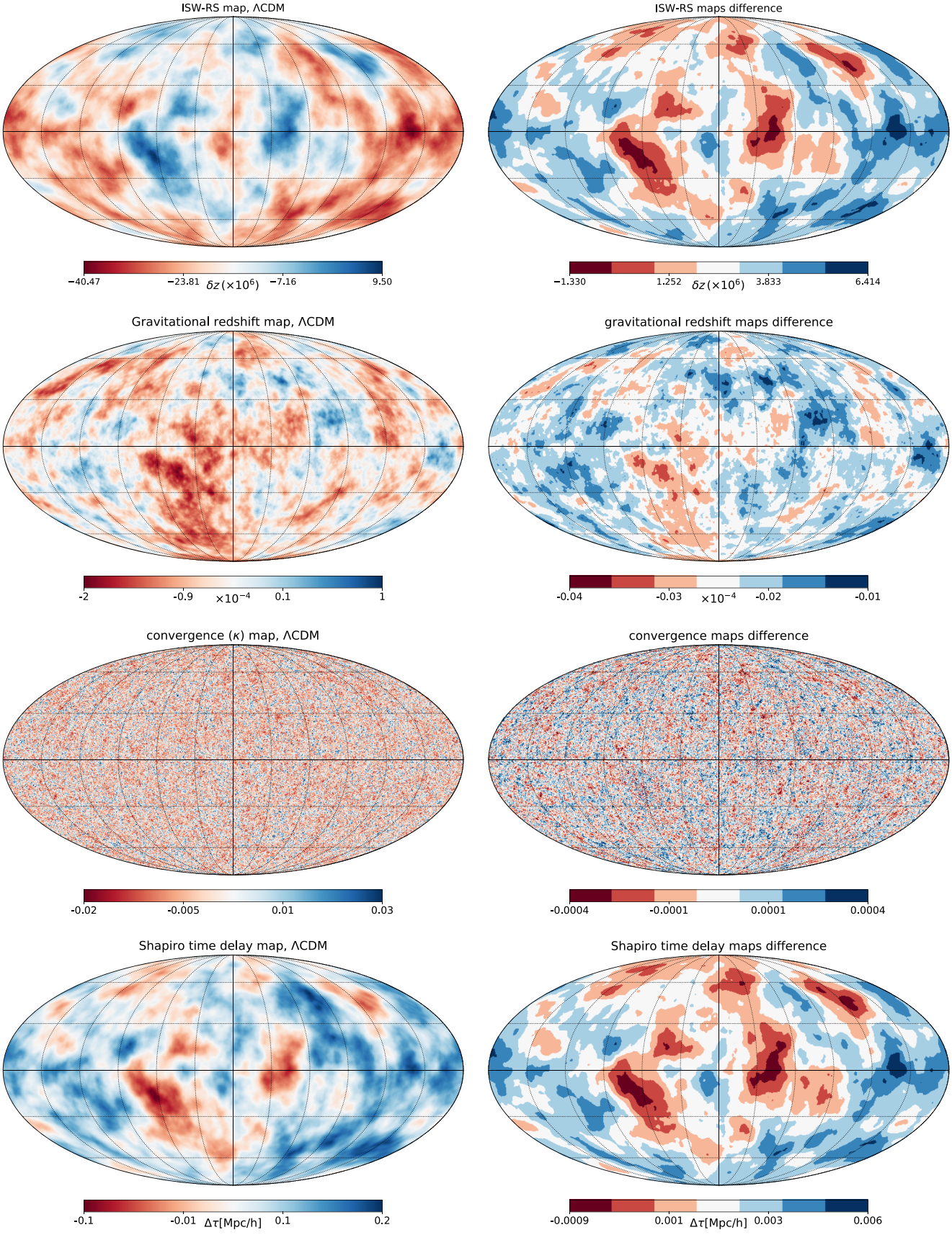

Figure 2. *Left:* Full-sky maps of the ISW-RS temperature anisotropy, gravitational redshift, convergence, and Shapiro time delay from a ΛCDM simulation using GEVOLUTION, integrated to $z \sim 0.8$, are shown. *Right:* Difference between the maps for *k*-essence with $c_s^2 = 10^{-7}$ and *k*-essence with $c_s^2 = 1$, both simulated with *k*-evolution. All simulations used the same seed to generate the random initial conditions and hence the difference maps indicate the importance of *k*-essence clustering.

The simulation boxes have a comoving size of $L = 4032\,\mathrm{Mpc}\,h^{-1}$. The fields evolve on a grid with $N_{\mathrm{grid}} = 4608^3$ grid points, and the matter phase space is sampled by $N_{\mathrm{pcl}} = 4608^3$ (i.e. about 100 billion) particles. We use the following cosmological parameters for all runs: The amplitude of scalar perturbations is set to $A_{\mathrm{s}} = 2.1 \times 10^{-9}$ at the pivot scale $k_{\mathrm{p}} = 0.05\,\mathrm{Mpc}^{-1}$, the scalar spectral index is $n_s = 0.96$, the Hubble parameter $h = 0.67$, cold dark matter and baryon densities are, respectively, $\omega_{\mathrm{cdm}} = \Omega_{\mathrm{cdm}}h^2 = 0.121\,203$ and $\omega_{\mathrm{b}} = \Omega_{\mathrm{b}}h^2 = 0.021\,996$, and the CMB temperature $T_{\mathrm{CMB}} = 2.7255$ K. We also include two massive neutrino species with masses $m_1 = 0.008\,689\,07$ eV and $m_2 = 0.05$ eV with temperature parameter $T_{\mathrm{C}\nu\mathrm{B}} = 1.951\,76$ K, as well as $N_{\mathrm{ur}} = 1.0196$ massless neutrinos (Adamek et al. 2017a). The effect of neutrino and radiation perturbations is approximated using the linear transfer functions from CLASS as described in Brandbyge & Hannestad (2009) and Adamek et al. (2017b), respectively. We only consider spatially flat universes, $\Omega_k = 0$, so that the dark energy density parameter is given by $\Omega_{\mathrm{DE}} = 1 - \sum_X \Omega_X$ where the sum goes over all species except dark energy. For the simulations where the dark energy is not a cosmological constant, we use a constant equation-of-state relation given by $w_0 = -0.9$ and $w_a = 0$.

The initial conditions for the simulations are set using the linear transfer functions from CLASS at $z = 100$ and all the simulations are run with the same seed number, which helps us to compare the results.

For our k-essence cosmology, we consider three different choices for the speed of sound: $c_{\mathrm{s}}^2 = 1$, 10^{-4}, and 10^{-7}. Strong non-linear clustering of the dark energy field is only expected in the last case, and to study this specific aspect, we run two separate simulations for this case. In one simulation, we use the code GEVOLUTION that approximates the dark energy perturbations by their solution from linear theory; see Hassani et al. (2019) for more details. In the other simulation, we use the code k-evolution in order to keep track of the dark energy field's response to the non-linear clustering of matter. For the higher values of the speed of sound, we only run k-evolution. We also do a reference run for the ΛCDM model with GEVOLUTION – here there is no difference between the two codes because dark energy perturbations are absent.

5 NUMERICAL RESULTS

In this section, we show the results of our numerical simulations. Once we have generated the maps with our pixel-based numerical integrator we use ANAFAST from the PYTHON package of HEALPIX to compute the angular power spectra and cross-power spectra. However, for the pencil beam maps that cover only about 5 per cent of the sky we instead use the pseudo-C_ℓ estimator of Wandelt, Hivon & Gorski (2001) and Szapudi et al. (2000) to obtain the power spectra in an unbiased way. To do so, we use the POLSPICE package to compute the angular power spectra and cross-power spectra of the masked maps.

5.1 Weak gravitational lensing

In the top panel of Fig. 3, the angular power spectra for the lensing convergence from k-evolution, GEVOLUTION, and CLASS integrating up to $\chi_{\mathrm{s}} = 2000\,\mathrm{Mpc}\,h^{-1}$ are shown, which corresponds to a source redshift of approximately $z = 0.85$. On the top the data points show the results for $\ell(\ell+1)C_\ell^\kappa$ of two simulations with $c_{\mathrm{s}}^2 = 10^{-7}$ and 1, as well as for ΛCDM. In addition, results for CLASS are shown for the case $c_{\mathrm{s}}^2 = 10^{-7}$ as dash–dotted and dotted lines, respectively,

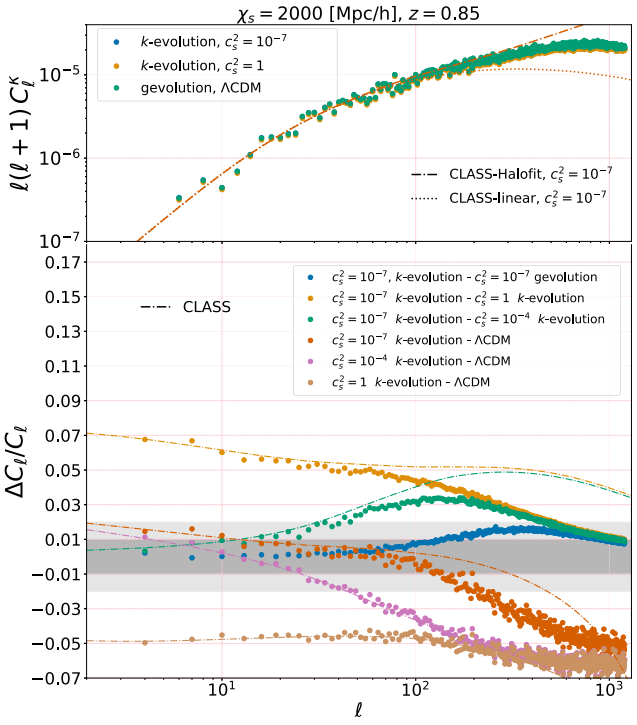

Figure 3. *Top panel:* The angular power spectra of the lensing convergence κ at a source distance of $\chi_{\mathrm{s}} = 2000\,\mathrm{Mpc}\,h^{-1}$ for some of our N-body simulations, as well as predictions from CLASS with and without the Halofit prescription. Based on the convergence test of Appendix A, we can trust the convergence spectrum here to $\ell \approx 200$, which is roughly where the dots start to deviate from the CLASS–Halofit curve. Relative spectra remain accurate to much higher ℓ. *Bottom panel:* Data points show the relative difference between the convergence power spectra from our N-body simulations for different models, whereas dashed lines represent the corresponding predictions from CLASS with Halofit, shown in matching colours. The blue points show the impact of k-essence non-linearities by comparing non-linear k-essence from k-evolution with its linear implementation in GEVOLUTION.

using linear theory alone or Halofit (Takahashi et al. 2012) to model the non-linear matter power spectrum.

The effect of matter non-linearities appears in the convergence power spectrum at $\ell \sim 100$ where both Halofit and N-body simulation data start to diverge from the linear prediction. In the bottom panel of Fig. 3, the relative difference between the convergence power spectra of different models is shown (we always keep χ_{s} fixed, which means that the source redshift can vary by a small amount depending on the background cosmology). This quantifies the effect of dark energy at different levels and can be compared to the prediction from CLASS. The data points show again the numerical results from our N-body simulations, whereas the CLASS/Halofit results for the same model comparisons are plotted as dashed lines using the same colours. Note that the comparison between k-evolution and GEVOLUTION for the case $c_s^2 = 10^{-7}$ has no corresponding prediction from CLASS, and quantifies the importance of the non-linear modelling of k-essence within the N-body simulations. To be specific, our convention is $\Delta C_\ell/C_\ell = (C_\ell^{(\text{data set 1})} - C_\ell^{(\text{data set 2})})/C_\ell^{(\text{data set 2})}$, where 'data set 1' and 'data set 2' are indicated in the legend of each figure.

At large scales, as expected, the results from CLASS and N-body simulations agree very well, while at smaller scales some deviations are seen. The deviation of the N-body results from the CLASS/Halofit prediction occurs mainly when there is dark energy clustering

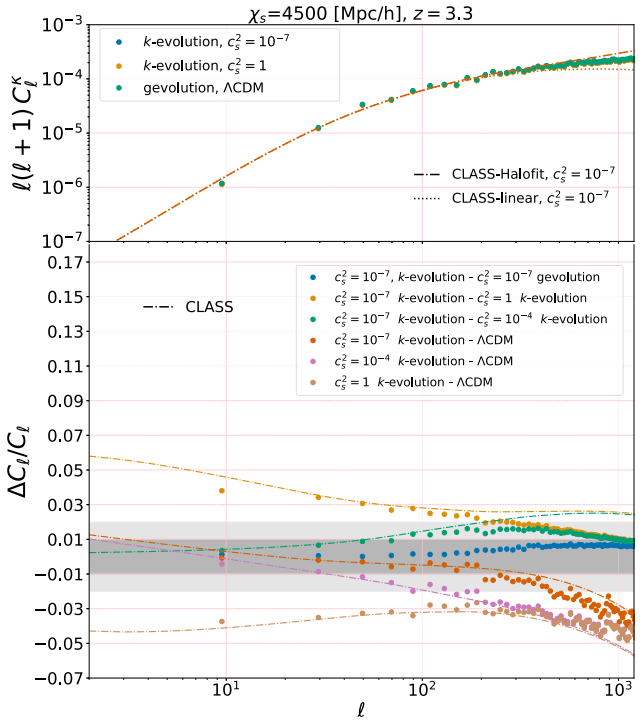

Figure 4. Same as Fig. 3, but for a source distance of $\chi_s = 4500$ Mpc h^{-1}, corresponding roughly to $z \approx 3.3$, and using N-body simulation data that cover ∼5 per cent of the sky. Again based on Appendix A, we can trust the dots in the top panel to $\ell \approx 500$, while the relative spectra shown in the bottom panel are again valid to higher ℓ.

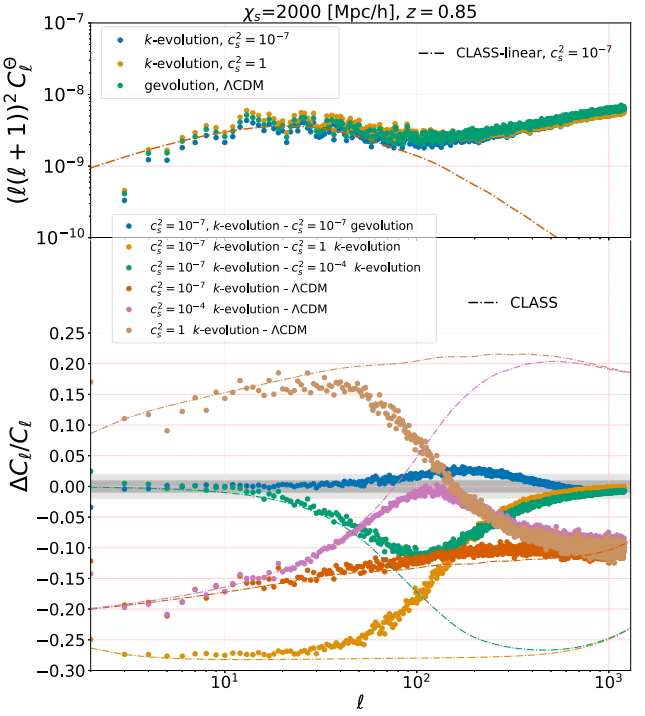

Figure 5. *Top panel:* The late-ISW-RS angular power spectra for different cosmologies integrating to $\chi_s = 2000$ Mpc h^{-1} are shown. Note that CLASS only predicts the linear ISW signal without any non-linear correction applied. The convergence study of Appendix A indicates that these spectra are reliable to $\ell \approx 500$, and the relative spectra are again valid to higher ℓ. *Bottom panel:* The relative difference between different models in the ISW-RS power spectra is shown. At large scales, the result from N-body codes agrees with CLASS; however, already at $\ell < 100$ the linear and non-linear curves diverge due to the non-linear RS effect.

that is more pronounced for the cases with low speed of sound. Indeed, comparing the case $c_s^2 = 1$ with ΛCDM, we find that the CLASS/Halofit prediction is accurate at least up to $\ell \sim 1000$, whereas for the lowest speed of sound, $c_s^2 = 10^{-7}$, significant disagreement between CLASS/Halofit and N-body simulations appears already for multipoles $\ell \gtrsim 100$. This is in complete agreement with our results in Hassani et al. (2020) where we show that CLASS/Halofit gives the right clustering function $\mu(k, z)$ for high speed of sound.

Our comparison between the two simulation methods (k-evolution and GEVOLUTION) for the case $c_s^2 = 10^{-7}$ shows that the non-linear response of k-essence to matter clustering produces an effect of ∼2 per cent in the convergence power spectrum at multipoles in the range of a few hundred.

According to Fig. 3, the effect of dark energy clustering can cancel the effect of the background evolution with $w_0 = -0.9$ on the weak-lensing signal at large angular scales: The ∼5 per cent suppression when going from ΛCDM to wCDM with $c_s^2 = 1$ is compensated by an amplification of similar size when going from $c_s^2 = 1$ to low speed of sound. The scale up to which this cancellation works is set by the sound horizon, and at very non-linear scales there is always some residual suppression. In our scenario, the cancellation happens only for the case $w_0 > -1$ when the linear growth rate is suppressed (see Fig. 1), while for the case with $w_0 < -1$, where the growth rate is enhanced compared to ΛCDM, the background evolution and the dark energy clustering effects would act in a similar way.

Fig. 4 is similar to Fig. 3 but shows results from the pencil beam map integrating to a higher source distance of $\chi_s = 4500$ Mpc h^{-1}, corresponding approximately to redshift $z = 3.3$. As we have access to only ∼5 per cent of the sky in this case, we have no information about the angular power spectra at low ℓ. The CLASS/Halofit and N-body simulation data agree better compared to the lower redshift results, as the scale where the finite resolution of the simulation affects the result is shifted to higher multipoles; see Appendix A (cf. also appendix C of Lepori et al. 2020). Moreover, the relative difference between the angular power spectra is less substantial compared to lower redshift result that comes from the fact that dark energy starts to dominate at lower redshift and integrating to higher redshifts therefore effectively dilutes the signal.

The overall signal amplitude for lensing is larger at higher redshift owing to the fact that it is an integrated effect. Thus, although the relative effect of dark energy clustering is lower at higher redshifts, the detectability of the signal is larger, and combining high- and low-redshift lensing data still significantly increases the signal-to-noise ratio.

5.2 ISW-RS effect

In Figs 5 and 6, the ISW-RS angular power spectra from our N-body simulations and CLASS are shown and the different dark energy models are compared in the bottom panel of each figure. The ISW-RS signal is very sensitive to the clustering of dark energy and also its background evolution. Comparing dark energy with low and high speeds of sound with ΛCDM, one finds a huge impact of ∼35 per cent at $z = 3.3$ and ∼30 per cent at $z = 0.85$ from dark energy clustering, which makes the ISW-RS signal an excellent probe of this model.

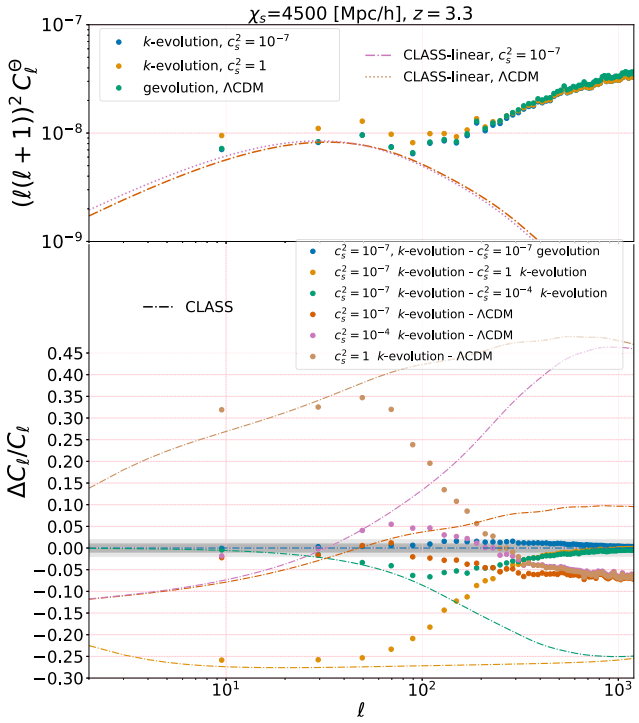

Figure 6. Same as Fig. 5, but for a source distance of $\chi_s = 4500$ Mpc h^{-1}, corresponding roughly to $z \approx 3.3$, and using N-body simulation data that cover ∼5 per cent of the sky. From the convergence study in the appendix, we conclude that these spectra are reliable over the full range of scales shown.

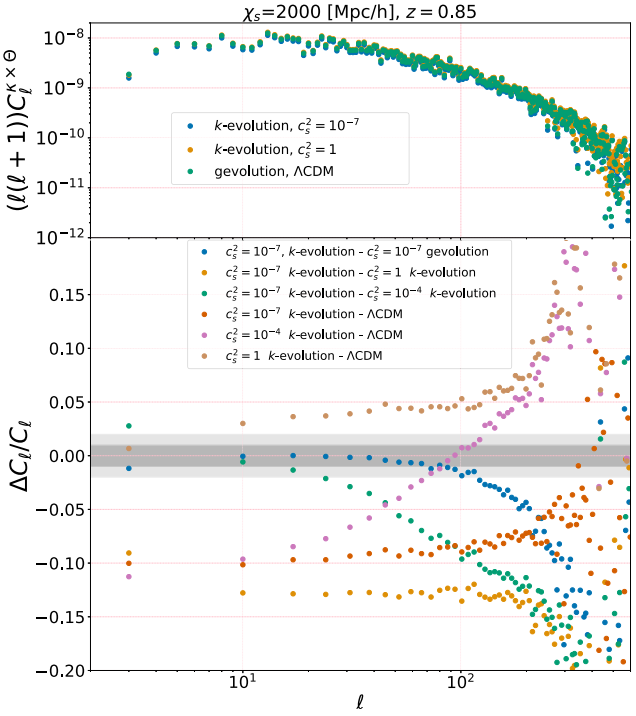

Figure 7. *Top panel:* The cross-power spectra of lensing convergence κ and ISW-RS integrated to a comoving distance of $\chi_s = 2000$ Mpc h^{-1} from k-evolution with two speeds of sound $c_s^2 = 10^{-7}$ and 1 are shown, together with our ΛCDM reference run. *Bottom panel:* The relative difference between the cross-power spectra for several models is shown.

It is also interesting to see that the non-linear RS effect starts to have an impact at larger scales than the scale of non-linearity in the lensing signal in Fig. 4 that is also observed and discussed in Cai et al. (2009) and Adamek et al. (2020). To verify that the non-linear RS indeed appears in lower moments, we design a numerical experiment to decrease the non-linear RS signal by decreasing A_s, the amplitude of scalar perturbations. This shifts the non-linear scale and allows us to separate the linear ISW effect from higher order corrections. Our numerical results, shown in Appendix B, verify that the non-linear RS effect is responsible for the deviation at lower ℓ compared to lensing. This is maybe not too surprising given that the lensing kernel suppresses contributions from the vicinity of the observer that would be projected dominantly to low multipoles.

The non-linear RS effect is not implemented in CLASS and as a result we a see power drop at $\ell \sim 100$ in the linear power spectra (top panels). Moreover, it is interesting to see that unlike the lensing power spectra, the effect of clustering dark energy and background evolution do not cancel each other in the ISW-RS power spectra and we obtain ∼−20 per cent relative difference between $c_s^2 = 10^{-7}$ and ΛCDM.

As seen in Fig. 6, the signal itself is stronger at higher redshift as it is an integrated signal. However, depending on the parameters the relative difference can change positively or negatively compared to the lower redshift comparison. This is because more linear ISW and less non-linear effect is accumulated at high redshift.

As explained in Section 3.2, the direct detection of ISW-RS signal is difficult and it is therefore usually detected indirectly, e.g. via cross-correlation with other quantities. As an example, we report the convergence-ISW-RS cross-power spectra in Figs 7 and 8. Fig. 9 shows the cross-correlation coefficient, i.e. the cross-power normalized to the rms of each individual signal. The effects of dark

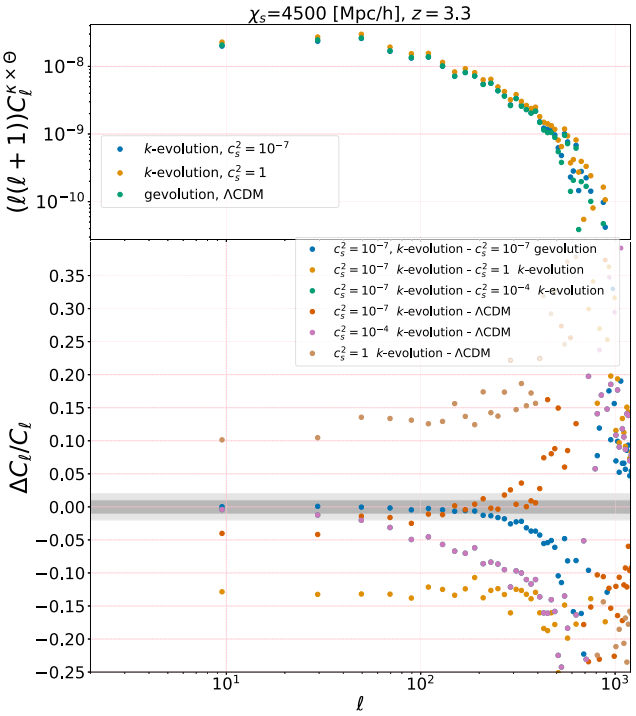

Figure 8. Same as Fig. 7, but for a source distance of $\chi_s = 4500$ Mpc h^{-1}, corresponding roughly to $z \approx 3.3$, and using N-body simulation data that cover ∼5 per cent of the sky.

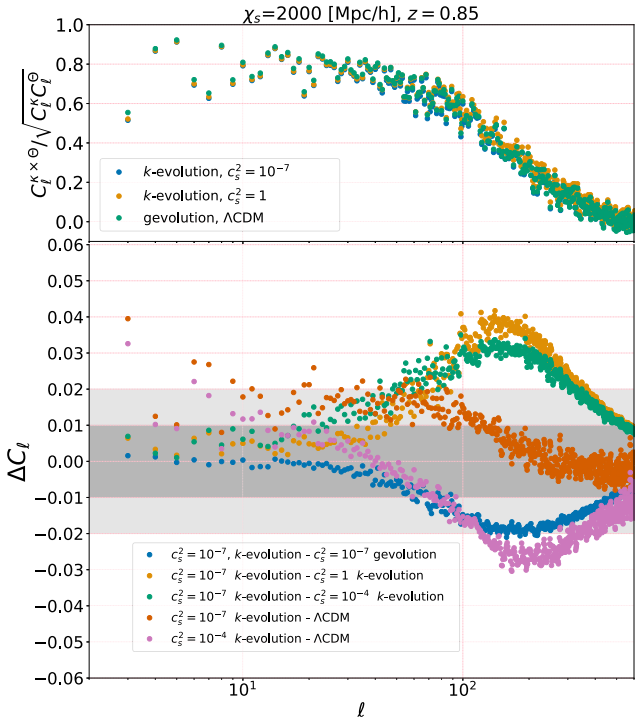

Figure 9. *Top panel:* The cross-correlation coefficient of lensing convergence κ and ISW-RS integrated to a comoving distance of $\chi_s = 2000$ Mpc h^{-1} for the results shown in Fig. 7. *Bottom panel:* Absolute difference in the cross-correlation coefficient for different models.

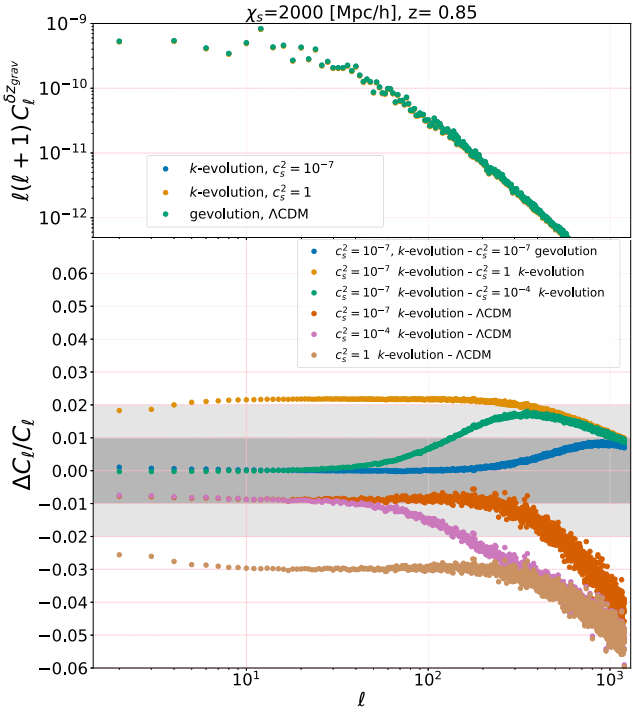

Figure 10. *Top panel:* The gravitational redshift angular power spectra of different cosmologies for a source plane at a comoving of distance $\chi_s = 2000$ Mpc h^{-1}. *Bottom panel:* The relative difference between the angular power spectra of the gravitational redshift in different cosmologies.

energy clustering and expansion history in the cross-power spectra follow similar trends as seen for the individual probes. Interestingly, the cross-correlation coefficient saturates to ∼0.8 at low ℓ almost independently of the dark energy model. This is because virtually all the effect is taken up by the normalization. However, the non-linear evolution is different in different models, which leads to an absolute change, ΔC_ℓ, in the cross-correlation coefficient of a few percentage points at high multipoles.

5.3 Gravitational redshift

In Fig. 10, the gravitational redshift angular power spectra for different scenarios are compared. The top panel shows $\ell(\ell+1)C_\ell^{\delta z_{\rm grav}}$ for three cases, and the bottom panel the relative difference between different angular power spectra. Like for the lensing signal, the effect of clustering and background almost cancels at large scales by coincidence: Comparing power spectra from dark energy with two different speeds of sound ($c_s^2 = 1$ and 10^{-7}), we find a difference of ∼2 per cent due to the clustering of dark energy. The relative difference between ΛCDM with wCDM with $c_s^2 = 1$ reaches ~ -3 per cent due to different background evolution. However, the difference between ΛCDM and k-essence with a low sound speed is only about 1 per cent. Fig. 10 also shows that the effect of non-linear dark energy clustering becomes visible once again for $\ell \gtrsim 100$, and is generally rather small, of the order of 1 per cent.

It should be noted that the angular correlation of the gravitational redshift will be very difficult to measure from large-scale structure observations. However, the line-of-sight correlations produce interesting signatures in redshift space, in particular a dipole in the correlation function of different matter tracers (Wojtak et al. 2011; Breton et al. 2019).

5.4 Shapiro time delay

In Fig. 11, the angular power spectra for the Shapiro delay signal are plotted. Our result for the relative spectra shows a similar pattern as for the gravitational redshift. The effects of dark energy clustering and dark energy background evolution have an ∼3 per cent effect on the Shapiro delay power spectrum that again cancel to a significant degree when combined. The non-linear dark energy clustering contributes again about a 1 per cent effect for $\ell \gtrsim 100$. We only report the Shapiro delay integrating to $\chi_s = 2000$ Mpc h^{-1}. The cosmological Shapiro time delay will be extremely challenging to measure. It contributes only to subdominant relativistic corrections in the redshift-space clustering, and we are not aware of a probe that easily isolates this effect.

6 CONCLUSION

We are, observationally speaking, in the golden era of cosmology and in the near future we will be able to put stringent constraints on dark energy and modified gravity models. However, to be able to unlock the full power of future observations we need to have a precise understanding of the non-standard scenarios well into the non-linear regime. The precise modelling of structure formation and cosmological observables covering linear to non-linear scales can be directly achieved using full N-body simulations.

In this work, we have presented the numerical results for the effect of clustering dark energy (specifically, the k-essence model) on the observables extracted from the gravitational potential, namely the weak gravitational lensing, ISW-RS, Shapiro time delay, and gravitational redshift. The observables discussed in this paper are calculated via a ray-tracing method integrating to the source redshifts $z \approx 0.85$ and 3.3 covering, respectively, a full-sky map and a pencil

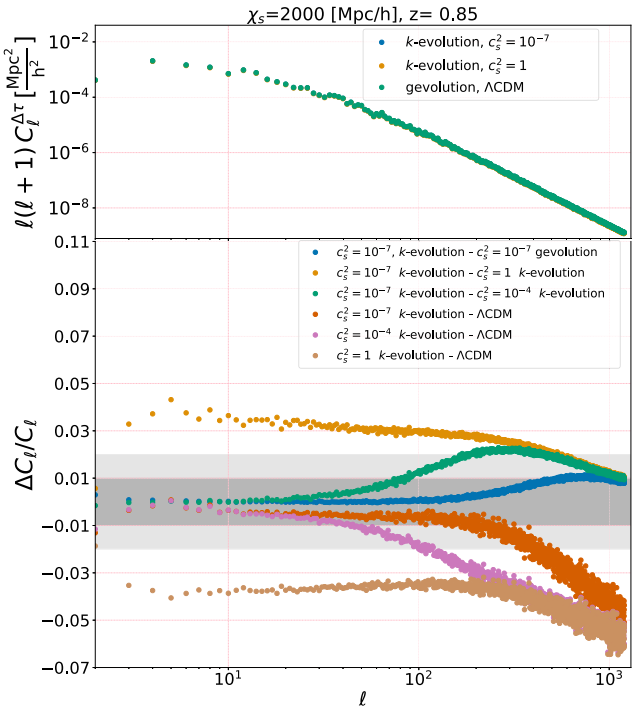

Figure 11. *Top panel:* The angular power spectra of Shapiro time delay integrated to a comoving distance of $\chi_s = 2000$ Mpc h^{-1} for different cosmologies. *Bottom panel:* The relative difference between Shapiro delay angular power spectra for different models.

beam in our simulations. Comparing results from the two *N*-body codes GEVOLUTION and *k*-evolution with the linear Boltzmann code CLASS, we are able to assess the different effects coming from the dark energy, specifically the effect from a different background evolution, from linear dark energy perturbations, and from the non-linear evolution of dark energy itself.

In summary, our numerical analysis of the angular power spectra of each observable shows that:

(i) The ISW-RS signal is the most powerful probe of different background evolution and the clustering of dark energy. Comparing dark energy with various speeds of sound ($c_s^2 = 10^{-7}$, 10^{-4}, and 1) with ΛCDM, one finds a significant impact of clustering dark energy on the ISW-RS angular power spectra reaching ∼35 per cent at $z = 3.3$ and ∼30 per cent at $z = 0.85$. Moreover, by comparing the linear ISW signal from CLASS with the non-linear signal from our *N*-body codes we are able to determine the scale and amplitude of the non-linear Rees–Sciama effect in the *k*-essence scenario.

(ii) The effect of dark energy on the weak gravitational lensing signal could reach ∼5 per cent. Interestingly, our numerical study shows that the effects of clustering of dark energy and background evolution can partially cancel each other.

(iii) The gravitational redshift and Shapiro time delay signals are less sensitive to the dark energy clustering and background evolution, as dark energy would change these signals at most by ∼3 per cent and ∼4 per cent, respectively, due to the different background evolution. An additional change by ∼2 per cent and ∼3 per cent can occur due to the clustering of dark energy.

Our numerical study shows how direct probes of the gravitational field, in particular weak lensing and the ISW-RS effect, can be used to constrain the nature of dark energy. It also highlights the relevance of including non-linear effects and provides a framework to model these effects in full *N*-body simulations. With this, we deliver some valuable guidance for the implementation of analysis pipelines that will be used to process the vast amount of upcoming observational data, with the aim to derive robust constraints on dark energy parameters.

Carbon footprint:

Our simulations consumed about 9800 kWh of electrical energy, which is equivalent to 1960 kg CO_2 with a conversion factor of 0.2 kg CO_2 kWh^{-1} from Vuarnoz & Jusselme (2018), table 2, assuming Swiss mix.

ACKNOWLEDGEMENTS

FH would like to thank Francesca Lepori for helping in the maps analysis, Mona Jalilvand for helping in making linear angular power spectra, and Shant Baghram for his comments about cross-correlating LSS data with ISW-RS signal. FH also would like to appreciate invaluable support from Jean-Pierre Eckmann during COVID-19 outbreak and his comments about our manuscript. FH and MK acknowledge funding from the Swiss National Science Foundation, and JA acknowledges funding by STFC Consolidated Grant ST/P000592/1. This work was supported by a grant from the Swiss National Supercomputing Centre (CSCS) under project ID s969. Part of the computations was performed at the University of Geneva on the Baobab cluster.

DATA AVAILABILITY

The *N*-body codes used for the simulations and data of this paper will be provided upon request to the corresponding author. The version of GEVOLUTION used in this work, together with the map-making tools, is available at this public repository: https://github.com/gevolution-code/gevolution-1.2.

REFERENCES

Abate A. et al., 2012, preprint (arXiv:1211.0310)
Abbott B. et al., 2017, ApJ, 848, L13
Adamek J., Daverio D., Durrer R., Kunz M., 2016a, J. Cosmol. Astropart. Phys., 07, 053
Adamek J., Daverio D., Durrer R., Kunz M., 2016b, Nat. Phys., 12, 346
Adamek J., Durrer R., Kunz M., 2017a, J. Cosmol. Astropart. Phys., 11, 004
Adamek J., Brandbyge J., Fidler C., Hannestad S., Rampf C., Tram T., 2017b, MNRAS, 470, 303
Adamek J., Clarkson C., Coates L., Durrer R., Kunz M., 2019, Phys. Rev. D, 100, 021301
Adamek J., Rasera Y., Corasaniti P. S., Alimi J.-M., 2020, Phys. Rev. D, 101, 023512
Ade P. et al., 2014a, A&A, 571, A17
Ade P. et al., 2014b, A&A, 571, A19
Ade P. et al., 2016a, A&A, 594, A13
Ade P. et al., 2016b, A&A, 594, A14
Ade P. et al., 2016c, A&A, 594, A21
Aghamousa A. et al., 2016, preprint (arXiv:1611.00036)
Alam S., Zhu H., Croft R. A. C., Ho S., Giusarma E., Schneider D. P., 2017, MNRAS, 470, 2822
Alishahiha M., Silverstein E., Tong D., 2004, Phys. Rev. D, 70, 123505
Alsing J., Kirk D., Heavens A., Jaffe A. H., 2015, MNRAS, 452, 1202
Amendola L., Kunz M., Sapone D., 2008, J. Cosmol. Astropart. Phys., 04, 013
Amendola L. et al., 2018, Living Rev. Relativ., 21, 2

Armendariz-Picon C., Damour T., Mukhanov V. F., 1999, Phys. Lett. B, 458, 209
Armendariz-Picon C., Mukhanov V. F., Steinhardt P. J., 2000, Phys. Rev. Lett., 85, 4438
Armendariz-Picon C., Mukhanov V. F., Steinhardt P. J., 2001, Phys. Rev. D, 63, 103510
Aubourg É. et al., 2015, Phys. Rev. D, 92, 123516
Bacon D. J., Refregier A. R., Ellis R. S., 2000, MNRAS, 318, 625
Baker T., Bellini E., Ferreira P., Lagos M., Noller J., Sawicki I., 2017, Phys. Rev. Lett., 119, 251301
Baldi M., 2012, Phys. Dark Univ., 1, 162
Barreira A., Li B., Hellwing W. A., Baugh C. M., Pascoli S., 2013, J. Cosmol. Astropart. Phys., 10, 027
Bartelmann M., Schneider P., 2001, Phys. Rep., 340, 291
Beck R., Csabai I., Rácz G., Szapudi I., 2018, MNRAS, 479, 3582
Becker M. R., 2013, MNRAS, 435, 115
Bellini E., Sawicki I., 2014, J. Cosmol. Astropart. Phys., 07, 050
Blanchard A. et al., 2019, preprint (arXiv:1910.09273)
Blas D., Lesgourgues J., Tram T., 2011, J. Cosmol. Astropart. Phys., 07, 034
Bonvin C., Durrer R., 2011, Phys. Rev. D, 84, 063505
Bonvin C., Caprini C., Durrer R., 2006, Phys. Rev. Lett., 97, 081303
Brandbyge J., Hannestad S., 2009, J. Cosmol. Astropart. Phys., 05, 002
Brando G., Koyama K., Wands D., 2020, preprint (arXiv:2006.11019)
Brax P., Davis A.-C., Li B., Winther H. A., Zhao G.-B., 2012, J. Cosmol. Astropart. Phys., 10, 002
Breton M.-A., Rasera Y., Taruya A., Lacombe O., Saga S., 2019, MNRAS, 483, 2671
Broadhurst T. J., Scannapieco E., 2000, ApJ, 533, L93
Cabass G., Gerbino M., Giusarma E., Melchiorri A., Pagano L., Salvati L., 2015, Phys. Rev. D, 92, 063534
Cai Y.-C., Cole S., Jenkins A., Frenk C., 2009, MNRAS, 396, 772
Cai Y.-C., Cole S., Jenkins A., Frenk C. S., 2010, MNRAS, 407, 201
Cai Y.-C., Li B., Cole S., Frenk C. S., Neyrinck M., 2014, MNRAS, 439, 2978
Cai Y.-C., Neyrinck M., Mao Q., Peacock J. A., Szapudi I., Berlind A. A., 2017, MNRAS, 466, 3364
Cappi A., 1995, A&A, 301, 6
Carbone C., Petkova M., Dolag K., 2016, J. Cosmol. Astropart. Phys., 07, 034
Challinor A., Lewis A., 2011, Phys. Rev. D, 84, 043516
Chiba T., Okabe T., Yamaguchi M., 2000, Phys. Rev. D, 62, 023511
Clifton T., Ferreira P. G., Padilla A., Skordis C., 2012, Phys. Rep., 513, 1
Copeland E. J., Kopp M., Padilla A., Saffin P. M., Skordis C., 2019, Phys. Rev. Lett., 122, 061301
Creminelli P., Vernizzi F., 2017, Phys. Rev. Lett., 119, 251302
Creminelli P., D'Amico G., Norena J., Vernizzi F., 2009, J. Cosmol. Astropart. Phys., 02, 018
Cusin G., Lewandowski M., Vernizzi F., 2018, J. Cosmol. Astropart. Phys., 04, 061
Dakin J., Hannestad S., Tram T., Knabenhans M., Stadel J., 2019, J. Cosmol. Astropart. Phys., 08, 013
de Putter R., Linder E. V., 2007, Astropart. Phys., 28, 263
Dossett J., Ishak M., 2013, Phys. Rev. D, 88, 103008
Durrer R., 2001, J. Phys. Stud., 5, 177
Ezquiaga J. M., Zumalacárregui M., 2017, Phys. Rev. Lett., 119, 251304
Fang W., Lu H., Huang Z., 2007, Class. Quantum Gravity, 24, 3799
Francis C., Peacock J., 2010, MNRAS, 406, 2
Frusciante N., Papadomanolakis G., 2017, J. Cosmol. Astropart. Phys., 12, 014
Gleyzes J., Langlois D., Piazza F., Vernizzi F., 2013, J. Cosmol. Astropart. Phys., 08, 025
Gorski K., Hivon E., Banday A., Wandelt B., Hansen F., Reinecke M., Bartelman M., 2005, ApJ, 622, 759
Granett B. R., Neyrinck M. C., Szapudi I., 2008, ApJ, 683, L99
Gubitosi G., Piazza F., Vernizzi F., 2013, J. Cosmol. Astropart. Phys., 02, 032
Handley W., Lemos P., 2019, Phys. Rev. D, 100, 043504
Hannestad S., Tu H., Wong Y. Y., 2006, J. Cosmol. Astropart. Phys., 06, 025
Hansen S. H., Hassani F., Lombriser L., Kunz M., 2020, J. Cosmol. Astropart. Phys., 01, 048
Hassani F., Lombriser L., 2020, MNRAS, 497, 1885
Hassani F., Baghram S., Firouzjahi H., 2016, J. Cosmol. Astropart. Phys., 05, 044
Hassani F., Adamek J., Kunz M., Vernizzi F., 2019, J. Cosmol. Astropart. Phys., 12, 011
Hassani F., L'Huillier B., Shafieloo A., Kunz M., Adamek J., 2020, J. Cosmol. Astropart. Phys., 04, 039
Hikage C. et al., 2019, PASJ, 71, 43
Hu W., Cooray A., 2001, Phys. Rev. D, 63, 023504
Jain B., Taylor A., 2003, Phys. Rev. Lett., 91, 141302
Jimeno P., Broadhurst T., Coupon J., Umetsu K., Lazkoz R., 2015, MNRAS, 448, 1999
Joyce A., Lombriser L., Schmidt F., 2016, Ann. Rev. Nucl. Part. Sci., 66, 95
Köhlinger F. et al., 2017, MNRAS, 471, 4412
Kang J. U., Vanchurin V., Winitzki S., 2007, Phys. Rev. D, 76, 083511
Khosravi S., Mollazadeh A., Baghram S., 2016, J. Cosmol. Astropart. Phys., 09, 003
Kim Y.-R., Croft R. A. C., 2004, ApJ, 607, 164
Koyama K., 2018, Int. J. Mod. Phys. D, 27, 1848001
Kunz M., Sapone D., 2007, Phys. Rev. Lett., 98, 121301
Laureijs R. et al., 2011, preprint (arXiv:1110.3193)
Lepori F., Adamek J., Durrer R., Clarkson C., Coates L., 2020, MNRAS, 497, 2078
Lewis A., Challinor A., 2006, Phys. Rep., 429, 1
Li B., Zhao G.-B., Teyssier R., Koyama K., 2012, J. Cosmol. Astropart. Phys., 01, 051
Li B., Barreira A., Baugh C. M., Hellwing W. A., Koyama K., Pascoli S., Zhao G.-B., 2013, J. Cosmol. Astropart. Phys., 11, 012
Li P., Dodelson S., Hu W., 2019, Phys. Rev. D, 100, 043502
Llinares C., Mota D. F., Winther H. A., 2014, A&A, 562, A78
Malquarti M., Copeland E. J., Liddle A. R., Trodden M., 2003, Phys. Rev. D, 67, 123503
Mandelbaum R., 2018, ARA&A, 56, 393
Martin J., 2012, C. R. Phys., 13, 566
Mead A. J., Peacock J. A., Heymans C., Joudaki S., Heavens A. F., 2015, MNRAS, 454, 1958
Nusser A., 2016, ApJ, 821, L2
Oyaizu H., Lima M., Hu W., 2008, Phys. Rev. D, 78, 123524
Peiris H. V., Spergel D. N., 2000, ApJ, 540, 605
Percival W. J., Cole S., Eisenstein D. J., Nichol R. C., Peacock J. A., Pope A. C., Szalay A. S., 2007, MNRAS, 381, 1053
Perlmutter S. et al., 1999, ApJ, 517, 565
Pratten G., Lewis A., 2016, J. Cosmol. Astropart. Phys., 08, 047
Puchwein E., Baldi M., Springel V., 2013, MNRAS, 436, 348
Rees M. J., Sciama D. W., 1968, Nature, 217, 511
Refregier A., 2003, ARA&A, 41, 645
Rendall A. D., 2006, Class. Quantum Gravity, 23, 1557
Reverberi L., Daverio D., 2019, J. Cosmol. Astropart. Phys., 07, 035
Riess A. G. et al., 1998, AJ, 116, 1009
Sachs R. K., Wolfe A. M., 1967, ApJ, 147, 73
Sadeh I., Feng L. L., Lahav O., 2015, Phys. Rev. Lett., 114, 071103
Sakstein J., Jain B., 2017, Phys. Rev. Lett., 119, 251303
Santos M. G. et al., 2015, Proc. Sci., Cosmology from a SKA HI Intensity Mapping Survey. SISSA, Trieste, PoS#019
Schmidt F., Lima M., Oyaizu H., Hu W., 2009, Phys. Rev. D, 79, 083518
Schmidt F., Leauthaud A., Massey R., Rhodes J., George M. R., Koekemoer A. M., Finoguenov A., Tanaka M., 2012, ApJ, 744, L22
Scranton R. et al., 2003, preprint (astro-ph/0307335)
Seljak U., 1996, ApJ, 460, 549
Shapiro I. I., 1964, Phys. Rev. Lett., 13, 789
Silverstein E., Tong D., 2004, Phys. Rev. D, 70, 103505
Spergel D. N. et al., 2003, ApJS, 148, 175
Spurio Mancini A., Reischke R., Pettorino V., Schäfer B. M., Zumalacárregui M., 2018, MNRAS, 480, 3725
Szapudi I., Prunet S., Pogosyan D., Szalay A. S., Bond J., 2000, preprint (astro-ph/0010256)

Takahashi R., Sato M., Nishimichi T., Taruya A., Oguri M., 2012, ApJ, 761, 152
Takahashi R., Hamana T., Shirasaki M., Namikawa T., Nishimichi T., Osato K., Shiroyama K., 2017, ApJ, 850, 24
Tegmark M. et al., 2004, Phys. Rev. D, 69, 103501
Tegmark M. et al., 2006, Phys. Rev. D, 74, 123507
Valogiannis G., Bean R., 2017, Phys. Rev. D, 95, 103515
Van Waerbeke L. et al., 2000, A&A, 358, 30
Verde L., Treu T., Riess A. G., 2019, Nat. Astron., 3, 891
Vuarnoz D., Jusselme T., 2018, Energy, 161, 573
Wandelt B. D., Hivon E., Gorski K. M., 2001, Phys. Rev. D, 64, 083003
Wei H., Cai R.-G., 2005, Phys. Rev. D, 71, 043504
Wojtak R., Hansen S. H., Hjorth J., 2011, Nature, 477, 567
Wyman M., Jennings E., Lima M., 2013, Phys. Rev. D, 88, 084029
Yoo J., Fitzpatrick A. L., Zaldarriaga M., 2009, Phys. Rev. D, 80, 083514
Zhao G.-B., Li B., Koyama K., 2011, Phys. Rev. D, 83, 044007
Zhu H., Alam S., Croft R. A., Ho S., Giusarma E., Leauthaud A., Merrifield M., 2019, preprint (arXiv:1901.05616)

APPENDIX A: CONVERGENCE TEST

In this appendix, we compare the results from our high-resolution simulations ($N_{\rm grid} = N_{\rm pcl} = 4608^3$) with some lower resolution ones ($N_{\rm grid} = N_{\rm pcl} = 2304^3$) for ISW-RS and convergence maps at both redshifts $z = 0.85$ and 3.3. This shows us at which scales the low-resolution simulations have converged to a certain numerical precision, and we can make a reasonable guess on how well we should be able to trust our final results from the high-resolution simulations.

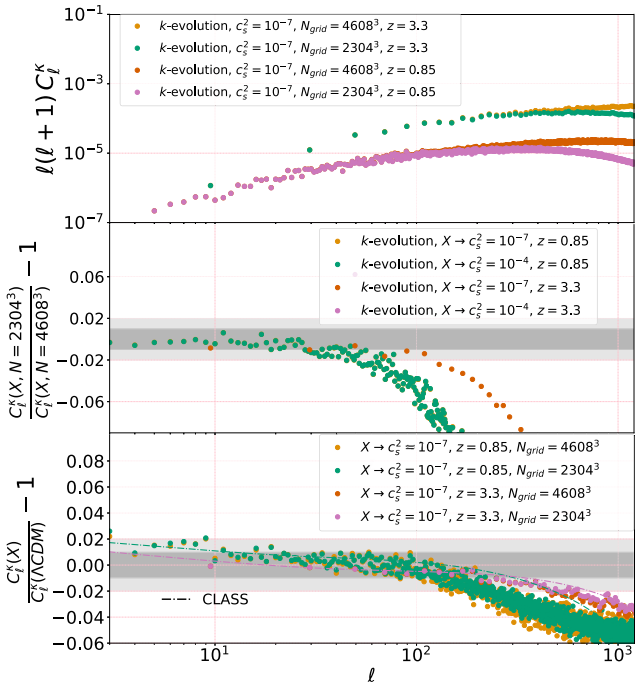

Figure A1. *Top panel:* We compare the convergence power spectra from two simulations with different resolutions, $N_{\rm grid} = N_{\rm pcl} = 4608^3$ and $N_{\rm grid} = N_{\rm pcl} = 2304^3$, at two source redshifts $z = 0.85$ and 3.3. *Middle panel:* The relative difference between the convergence power spectra of the same cosmology but different resolutions of the simulations is shown. This gives us an estimation of the finite resolution error on the convergence angular power spectra. The grey areas show 1 per cent and 2 per cent numerical agreement. *Bottom panel:* Comparing the relative change in the convergence power spectra between ΛCDM and k-essence cosmology with the speed of sound $c_s^2 = 10^{-7}$ from two simulations with different resolutions, $N_{\rm grid} = N_{\rm pcl} = 4608^3$ and $N_{\rm grid} = N_{\rm pcl} = 2304^3$, at source redshifts $z = 0.85$ and 3.3. The dashed lines show the linear theory prediction obtained from CLASS. The agreement across different resolutions shows that one can trust the relative change of power spectra at much higher multipoles than is the case for the individual power spectra themselves.

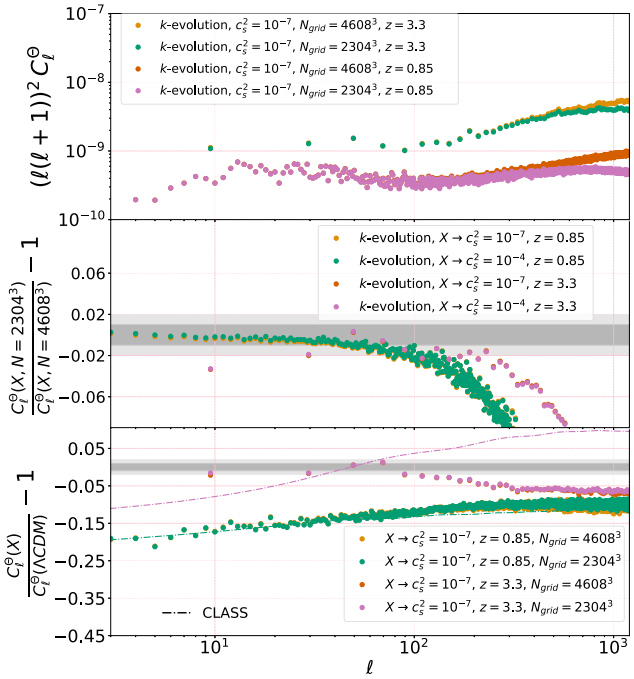

Figure A2. *Top panel:* We compare the ISW-RS angular power spectra from two simulations with different resolutions, $N_{\rm grid} = N_{\rm pcl} = 4608^3$ and $N_{\rm grid} = N_{\rm pcl} = 2304^3$, at two source redshifts $z = 0.85$ and 3.3. *Middle panel:* The relative difference between the ISW-RS angular power spectra of the same cosmology but different resolutions of the simulations is shown. *Bottom panel:* The relative difference of ISW-RS angular power spectra between the k-essence cosmology with $c_s^2 = 10^{-7}$ and ΛCDM for two different spatial resolutions $N_{\rm grid} = N_{\rm pcl} = 4608^3$ and $N_{\rm grid} = N_{\rm pcl} = 2304^3$ at two source redshifts $z = 0.85$ and 3.3. The dashed lines show the linear theory prediction obtained from CLASS. Like Fig. A1, this figure shows that the finite resolution effect is cancelled significantly in the relative changes of the angular power spectra.

According to Fig. A1, the convergence angular power spectrum is converged to within 5 per cent up to $\ell \sim 100$ and 250, respectively, for a source redshift of $z = 0.85$ and 3.3. Assuming that a factor of 2 in spatial resolution translates to a similar improvement in the angular resolution, we may want to trust our final results up to $\ell \sim 200$ and 500, respectively, maintaining an ∼5 per cent absolute convergence threshold. However, the leading-order error due to finite resolution is usually almost independent of cosmology, which means that it cancels out to high accuracy when taking ratios. Whenever we show relative changes, we therefore expect much better numerical convergence. In the bottom panel of Fig. A1, we show the relative change between ΛCDM and wCDM convergence power spectra for two different spatial resolutions. In these relative spectra, the curves with different resolutions agree at all ℓ shown, explicitly demonstrating the cancellation of the finite resolution error in the relative power spectra.

Considering Fig. A2, we can draw similar conclusions for the numerical convergence of the ISW-RS signal. The 5 per cent error is reached at somewhat higher ℓ, which means that we may be able to

trust our final results up to $\ell \sim 400$ and 800 for the two redshift values if we apply the same requirement on absolute numerical convergence. Also, according to the bottom panel of the figure the relative spectra from the two different resolutions are consistent so that we can trust the ISW-RS relative difference power spectra at all scales of interest. We emphasize again that the results shown in this paper were obtained using the higher resolution simulations.

APPENDIX B: NON-LINEAR REES–SCIAMA EFFECT

In this appendix, we quantify in more detail the contribution of the non-linear Rees–Sciama effect to the ISW-RS signal at low multipoles $\ell \lesssim 100$. To this end, we run additional simulations for the wCDM cosmology with $c_s^2 = 1$ and for ΛCDM, but with the power of primordial perturbations, A_s, reduced by two orders of magnitude. As a result, the evolution is almost linear up to much smaller scales, bringing the numerical result for the ISW-RS signal into very good agreement with the calculation of the linear ISW alone as performed by CLASS. This can be clearly seen in the left-hand panel of Fig. B1 where the simulations with low A_s remain consistent with the prediction from CLASS well beyond $\ell \sim 100$. Taking the ratio of spectra from the simulations with the standard value of A_s to the ones with low A_s, we can therefore get a good estimate of the fractional contribution of the Rees–Sciama effect. The result of this analysis is shown in the right-hand panel of Fig. B1, which suggests that the Rees–Sciama effect changes the signal by a few per cent at very low $\ell \lesssim 20$, and then gradually ramps up to reach an ∼100 per cent correction at around $\ell \sim 100$. Interestingly, the non-linear corrections are systematically larger in ΛCDM, which can be explained by the fact that the linear growth rate is slightly suppressed in our wCDM cosmology; see Fig. 1. This, in turn, is expected to lead to a corresponding relative suppression of second-order corrections like the Rees–Sciama effect.

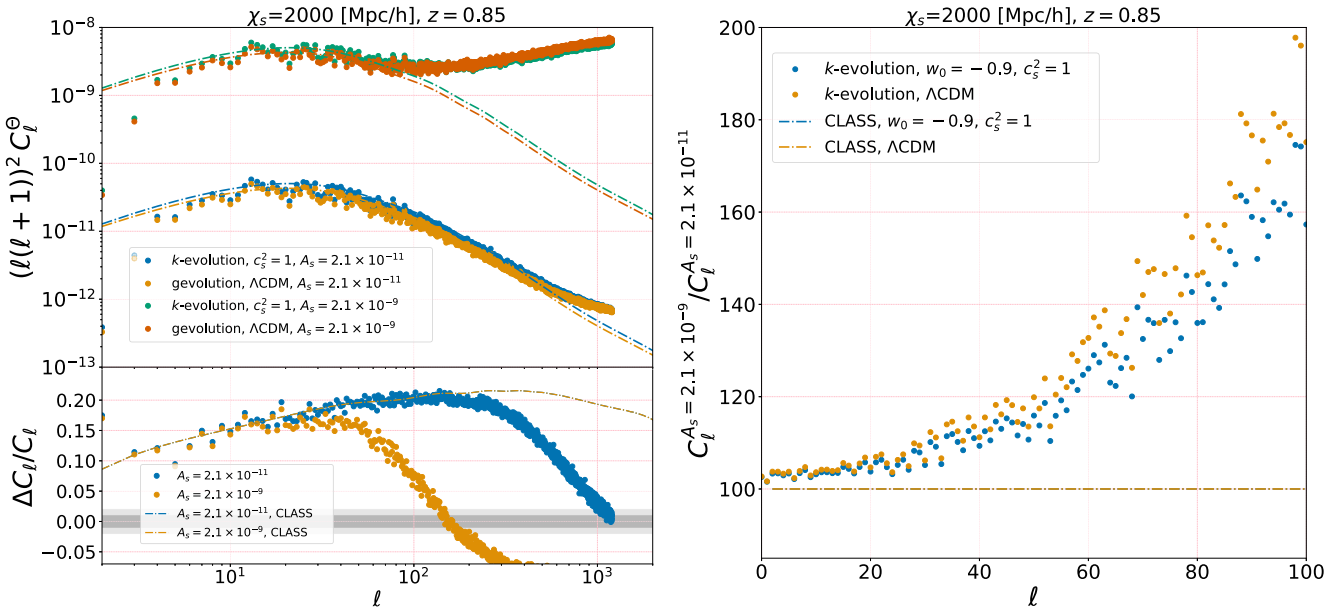

Figure B1. *Left:* The ISW-RS angular power spectra for two different cosmologies ($w_0 = -0.9$, $c_s^2 = 1$) and ΛCDM with standard and low value of A_s, the amplitude of scalar perturbations. *Right:* The ratios of the ISW-RS signal from high value of A_s to low value of A_s are compared. The linear result is constant at all scales, and is simply the ratio of the two values of A_s. The fractional contribution of the Rees–Sciama effect depends on w_0 mainly because of suppressed growth and the corresponding shift of the non-linear scale with respect to ΛCDM.

This paper has been typeset from a TEX/LATEX file prepared by the author.